MINERAL-MICROBE INTERACTIONS AND BIOMINERALIZATION OF SILICEOUS SINTERS AND UNDERLYING ROCK FROM JENN'S POOLS IN THE UZON CALDERA, KAMCHATKA, RUSSIA

by

JENNIFER E. KYLE

Under the Direction of Paul Schroeder

ABSTRACT

Siliceous sinters were collected from two high temperatures, disaerobic, reducing terrestrial hot springs from the Uzon Caldera, Kamchatka, Russia for the purpose of characterizing microbe-mineral interactions, and biomineralization of the sinters, associated microbial mats, and underlying rocks. X-Ray Diffraction (XRD) and Thermogravimetric Analysis (TGA) were used to determine the major mineral phases present within the rocks. High resolution analysis through electron microscopy was used to characterize minor mineral phases present within the rocks and microbial mats, and to analyze microbe-mineral interactions and biomineralization of prokaryotes. Opal-A was the dominant mineral phase comprising the siliceous sinter. Clay alteration of the underlying rocks of vent 1 was due to the sulfate-type waters not found in vent 2. Microbe-mineral interactions were most commonly associated with iron-bearing mineral phases since the can be directly used for metabolic processes. Biological induced mineralization through extracellular silicification was the only form of biomineralization with the exception ferrihydrite and pyrite mineralized cells. These microbial signatures offer clues to how the earliest microorganism on Earth may have preserved and where they derived their energy.

INDEX WORDS: Siliceous sinters; Microbe-mineral interactions; Biomineralization; Microbial signatures; Terrestrial hot springs; Kamchatka

MINERAL-MICROBE INTERACTIONS AND BIOMINERALIZATION OF SILICEOUS SINTERS AND UNDERLYING ROCK FROM JENN'S POOLS IN THE UZON CALDERA, KAMCHATKA, RUSSIA

by

JENNIFER E. KYLE

B.S., The University of Georgia, 2003

A Thesis Submitted to the Graduate Faculty of The University of Georgia in Partial Fulfillment of the Requirements for the Degree

MASTERS OF SCIENCE

ATHENS, GEORGIA

2005

MINERAL-MICROBE INTERACTIONS AND BIOMINERALIZATION OF SILICEOUS SINTERS AND UNDERLYING ROCK FROM JENN'S POOLS IN THE UZON CALDERA, KAMCHATKA, RUSSIA

by

JENNIFER E. KYLE

Major Professor: Paul Schroeder

Committee: Christopher Romanek
Andrew Neal

Electronic Version Approved:

Maureen Grasso
Dean of the Graduate School
The University of Georgia
August 2005

ACKNOWLEDGMENTS

I would like to thank my major advisor Paul Schroeder for all his time, support, encouragement, enthusiasm, and the opportunity to work on this project.

I would also like to thank my committee members, Chris Romanek and Andy Neal, and Doug Crowe for their continuous support, comments, and time.

This work was funded by a grant from the National Science Foundation's Microbial Observatory, NSF MO 0238407, and the Department of Geology's Wheeler-Watts fund.

TABLE OF CONTENTS

Page

LIST OF TABLES

LIST OF FIGURES

CHAPTER 1

INTRODUCTION

Terrestrial hot springs of near neutral pH are active sites of siliceous sinter formation throughout the world (Fournier et al. 1985; Renaut et al. 1998; Hedianita et al. 2000; Braunstein and Lowe 2001; Konhauser et al 2001; Mountain et al. 2003; Jones and Renaut 2004). Recently, siliceous sinter deposits have attracted the attention of geologists and microbiologist because they can form in high temperature, anoxic environments, similar to the conditions of early Earth. The search for evidence of life on early Archean Earth, and other planets and moons, have led many researchers to study sinters given that they contain active sites of microbial activity and biominearlization, leaving a morphological and mineralogical signature within them. Siliceous sinters from two springs in Winding Stream in the Uzon Caldera were collected in August and September of 2003 and 2004 for the purpose of characterizing mineral-microbe relationships through the identification of mineral assemblages in the sinters and underlying rocks, and the characterization of various modes of biomineralization.

Siliceous Sinter Formation and Maturation

Siliceous sinter formation is a three step process: (1) the solution must be supersaturated with respect to amorphous silica, (2) opal-A must nucleate and grow a colloidal suspension, and (3) deposition begins as suspended opal-A agglomerate and cement (Rimstidt and Cole 1983). Geothermal solutions become supersaturated with respect to amorphous silica as hot undersaturated fluids dissolve silicates within the host rock. As the fluid ascends and cools, silica precipitates at the surface (Rimstidt and Cole 1983). The presence of sinter deposits

implies a subsurface silica reservoir temperature of greater than 175°C (Fournier and Rowe 1966).

Nucleation for sinter formation is believed to be a heterogeneous process. In high temperature hot springs, supersaturation and excess Gibbs free energy (ΔG) are not sufficient to induce homogeneous nucleation (Rimstidt and Cole 1983). Instead, opal-A nucleates on pre-existing substrates, either organic or inorganic, and this lowers the activation energy required for nucleation. Opal-A is the initial polymorph in siliceous sinter formation because it requires the least activation energy for nucleation compared to other silica polymorphs. Because opal-A is a relatively disordered silica polymorph few constaints are placed on the alignment of the crystal lattice within an underlying template (Rimstidt and Cole 1983), thus allowing silica to preferentiallyprecipitate.

Once sinters begin to form, continued growth results as silica is precipitated in one of four ways: (1) by alternating submergence and exposure, (2) vertical growth by capillary action, (3) by evaporation in splash zones (Renaut et al. 1998), and (4) through spicular growth caused by an increased concentration of microbial filaments at the spicule tips (Cady and Farmer 1996). Microbial cell walls and exopolymeric substances (EPS) often act as a template towards sinter formation due to the low energy barrier towards nucleation.

Once formed, opal-A undergoes a slow dissolution/reprecipitation process to form more ordered opal-CT (Rice et al. 1995). Opal-CT recrystallizes to form opal-C which will eventually form quartz (Rice et al. 1995). This entire transformation from opal-A to quartz can take up to 50,000 years. The overall process results in an increase in crystal ordering and density, and a decrease in water content and porosity (Herdianita et al. 2000).

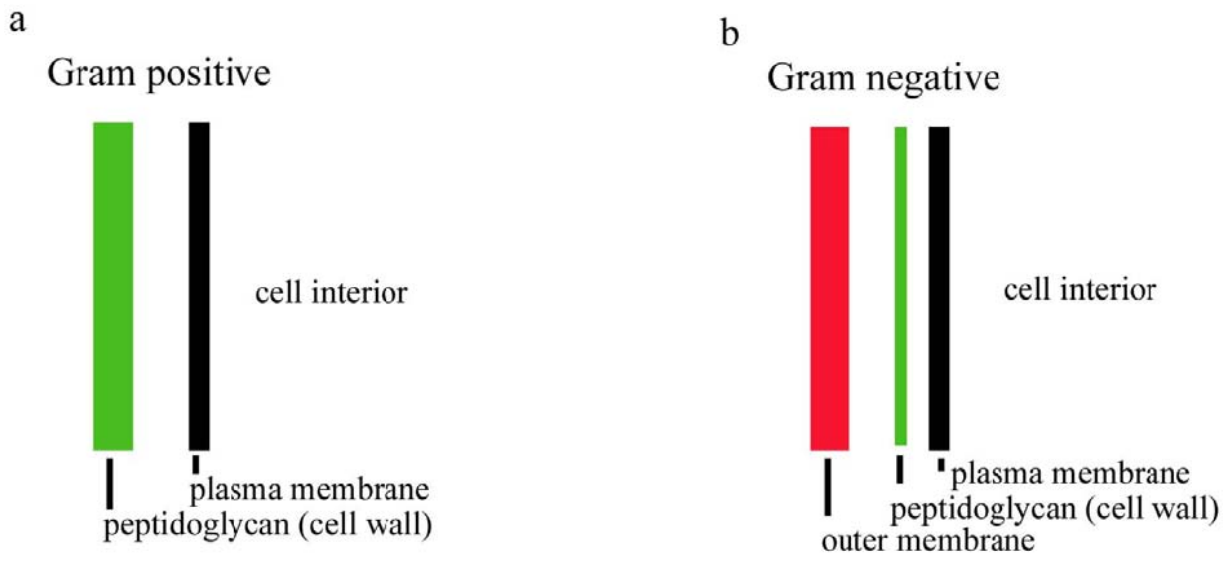

Figure 1. Simplified structure of the two major types of bacteria. Gram positive (a) bacteria contain a thick peptidoglycan layer, separated from the plasma (cell) membrane by the periplasmic space. Gram negative (b) bacteria contain a thin peptidoglycan layer that lies between the outer membrane (and periplasmic space) and the plasma (cell) membrane. Modified from Prescott et al. (2000).

Biomineralization

Differences in bacteria have been shown to influence the degree of biomineralization occurring at cell surfaces (Westall et al. 1995). This difference is due to the structural composition of the cell wall of two major groups of bacteria: gram positive and gram negative, identified by the retention of a gram stain. Gram positive bacteria have a thick cell wall composed of a peptidoglycan layer that is located outside the plasma membrane and periplasmic space, whereas gram negative bacteria have a much thinner peptidoglycan layer that resides between the plasma membrane and the outer membrane (Fig. 1; Prescott et al. 2002). Peptidoglycan functions as a protective barrier and helps keep the structural integrity of the cell. The abundant carboxyl groups of peptidoglycan gives the cell wall an overall negative charge. In gram positive bacteria, the peptidoglycan layer contain teichoic acids that are rich in phosphoryl groups, contributing the net negative charge of the cell (Prescott et al. 2003). Gram

negative bacteria do not have teichoic acids but lipopolysaccharides (LPS) on the surface of the outer membrane that are highly anionic (phosphate-rich; Frankel and Bazylinski 2003). This net negative charge on the cell surface can cause ions in the surrounding environment to become attracted to the cell, resulting in the mineralization of the outer cell.

The form of mineralization described above is called biologically induced mineralization (BIM; Lowenstam 1981). Biologically inducted mineralization is unintended and uncontrolled, and occurs as a consequence of interaction between the cell surface and/or metabolic byproducts and the surrounding environment (Frankel and Bazylinski 2003). Anaerobic environments are common areas for BIM since bacteria tend to respire with sulfate and/or other metals, and produce reactive sulfide and reduced forms of metals that commonly result in mineral formation (Frankel and Bazylinski 2003).

The second form of mineralization is termed biologically controlled mineralization (BCM; Lowenstam 1981; Mann 1983) and it occurs as the organism exhibits intended control over mineral formation (Frankel and Bazylinski 2003). The mineral phases formed are believed to be under specific genetic and/or biochemical control by the organism (Bazylinski and Frankel 2003). Magnetite formed by magnetotactic bacteria are an example of BCM. The magnetite formed within the intracellular vesicles are rarely contain trace elements, are about 35 to 120 nm is size, limited in morphology, and highly structured (Bazylinski and Frankel 2003). Although it can be difficult to discriminate between BIM and BCM, some relationships exist. Biological induced minerals are heterogeneous such that composition, size, structure, morphology, and water content can differ, whereas for BCM these characteristics are not as diverse and more restricted in chemistry and structure (Frankel and Bazylinski 2003).

A common form of BIM within terrestrial hot springs are extracellular silicified molds.

These morphological microbial remnants are found throughout the world in sinter deposits such as Taupo Volcanic Zone, New Zealand (Jones et al. 2001; Jones et al. 1997; Jones and Renaut 1996), Lorburu hot springs, Kenya Rift Valley (Renaut et al. 1998), Yellowstone National Park, USA (Cady and Farmer 1996), and Strokkur Geyser outflow, Iceland (Schultze-Lam et al. 1995).

Bacterial cells commonly act as a passive template during silica formation and two mechanisms have been proposed for how silica binds to the surface of bacterial cell. The first is direct contact between the dissolved silica and the microbial cell wall (Mera and Beveridge 1993; Westall et al. 1995), and the second involves the formation of a metal ion bridge between the cell wall and silica in solution (Fortin and Beveridge 2000; Mera and Beveridge 1993). Direct nucleation on the cell wall occurs as negatively charged domains of silica ions bind to electropositive functional groups, such as $NH4^{+}$, on the surface of live bacteria (Mera and Beveridge 1993). Another possible mechanism is that of silicic acid hydroxyl groups sorbed directly to the bacterial cell wall (Westall et al. 1995) through hydrogen binding (Ferris et al. 1988). Solid state ^{29}Si nuclear magnetic resonance studies conducted by Perry and Mann (1989) found that no Si-O-C peak existed implying that the interactions are largely noncovalent and may involve hydrogen binding.

Given that positively charged regions on the outside of cell wall are not common, an alternative mechanism involves the formation of a metal ion bridge binding to negative functional groups within the cell wall of bacteria. Negative functional carboxyl and phosphoryl groups, electrostatically bind metals to the cell wall (Fortin and Beveridge 2000), which in turn bind silica to the cell surfaces (Mera and Beveridge 1993). The initial binding of metals, especially iron, to the cell wall inactivates autolytic enzymes (Ferris et al. 1988) enabling greater preservation of the original structure of the microorganism. After initial sorption, silica

continues to precipitate around the cell abiotically causing a thickening of the silica crust (Konhauser et al. 2003). The continued growth of silica around the cells can entomb the microbe over time, leaving behind a silicified tube as the only textural signature of the microbes' existence.

Early Earth and Mars signatures of life

Conditions on early Archean Earth (and possibly Mars) may have been very similar in that both were high temperature, reducing, anoxic environments where life is thought to have originated from aquatic habitats as chemolithotrophic thermophilic anaerobes (Westall et al. 2005). The search for the first signs of life on Earth has proven difficult and arduous, undergoing rigorous criticism. Many abiotic processes (i.e. metamorphism, hydrothermal activity) can mimic microstructures interpreted as early Archean prokaryotic microfossils. Currently, only a few samples are considered probably evidence of past life. The earliest evidence of life on Earth dates back 3.8 Ga in the Isua Supracrustal belt (ISB) in southern West Greenland (van Zuilen et al. 2000). Turbidite beds deposited within an oceanic setting of the western region of the ISB contain carbon which is believed to be originally deposited as particulate organic matter (Rosing 1999). The micron sized graphite grains have δ^{13}CPDB values of -17 ‰ to -19 ‰ which are within the range of biologically reduced carbon (Rosing 1999; van Zuilen et al. 2000). The graphite was not found in association with siderite or magnetite or other iron-carbonate phases in which graphite can be produced by an inorganic disproportionation reaction (van Zuilen et al. 2000).

The oldest microfossils of the Barberton Sequence, Africa are located in the Archean stromatolitic units of the Onverwacht and Fig Tree Groups 3.5 to 3.3 Ga (Altermann 2001). Within the Hooggenoeg (3.47-3.44 Ga) and Kromberg Formation (3.42-3.33 Ga) of the

Onverwacht Group, opaque and hollow sheath-like filaments 1.0 μm to 2.5 μm, found in stromatolitic laminations, and spheroids 10 μm to 50 μm in diameter resembled bacterial filaments and coccoidal bacteria or spores, respectively (Walsh and Lowe 1985; Walsh 1992). These bacterium-like fossils were found associated with pyrite, the filaments were relatively constant in diameter along their length, cross-cutting crystal domains, and found parallel to bedding planes as if compressed during compaction of the unit (Walsh and Lowe 1985). One area from the Kromberg Formation had an isotopic δ^{13}CPDB value of –27 ‰ (Westall et al. 2001) which is in the range of biologically reduced carbon.

The Warrawoona Group of Western Australia also contains microfossils approximately the same age as the Onverwacht Group in South Africa. The microfossils in the Warrawoona Group were found within carbonaceous cherts of the Towers (3.4 Ga) and Apex Basalt Formation (3.34-3.33 Ga; Schopf and Packer 1987). The Australian microfossils have been suggested to represent a cyanobacterial predecessor (oxygen producing photoautotroph) due to morphological similarities with modern cyanobacteria, which included septae, cell dimensions, and sinuous and unbranched segments (Schopf and Packer 1987; Schopf 1993). Later investigations by Brasier et al. (2002) interpreted the proposed microfossils to be inorganic forms of hydrothermal quartz. Schopf and Packer (1987) and Schopf (1993) provided evidence that oxygen-producing cyanobacteria lived in the early Archean. Their research has been reexamined, and found that if the microfossils were indeed authentic, they were more likely to be from hyperthermophilic bacteria not cyanobacteria (Brasier et al. 2002).

Contrary to the photoautotrophic debate for the earliest known microorganisms on Earth, early evidence for bacterial sulfate reduction exists in sulfide grains from 3.47 Ga old barite crystals, which have δ^{34}S values as high as 21.1 ‰ (mean value of 11.6 ‰; Shen et al. 2001).

Although these $\delta^{34}S$ values can be produced abiotically, Shen et al. (2001) considered the possibility unlikely. Microscopic sulfides found along the original gypsum crystal faces indicated the sulfide formed at low temperatures when the original gypsum was still present discounting hydrothermal or metamorphic origins of the sulfides (Shen et al. 2001). Currently many known sulfate-reducers thrive below 70° C, the early Archean predecessor must have been mesophilic or moderate thermophile because gypsum and associated sulfides formed below 60° C (Shen et al. 2001).

Evidence for past life on Mars has also been under great debate given that many biologically interpreted features could also result from an abiotic origin. The meteorite ALH84001 has been a primary focus for evidence of past life on Mars (McKay et al. 1996). Four characteristics of this meteorite contain evidence for past life including (1) carbonate globules forming at low temperatures (< 100° C) (Romanek et al. 1994), (2) the presence of mineral grains (magnetite and iron sulfides) with characteristics similar to those formed by bacteria, (3) presence of reduced carbon (McKay et al. 1996), and (4) features within the carbonates that are morphologically similar to biogenic structures on Earth (McKay et al. 1996). McKay et al. (1996) suggests that collectively these observations suggest a biogenic origin for some of the features in the meteorite, although individually, an abiotic origin can be interpreted for each observation.

Given the interest in the evolution of the first organisms on Earth, and possibility of life on other planets and moons, eight criteria have been suggested to identify evidence of past life: (1) geologic context of the sample, (2) age and stratigraphic location within the parent rock, (3) evidence of cellular morphology, (4) structural remains of colonies, communities, or cells, (5) evidence of biominerals showing chemical or mineral disequilibrium, (6) stable isotope patterns

unique to life, (7) evidence of organic biomarkers, and (8) evidence of features indigenous to the sample (Gibson et al. 2001). The aim of this present project is not to establish the above characteristics in this study, but to note the above criteria are difficult to satisfy even when studying modern analogs of microbial biomineralization and preservation.

Geology of the Uzon

The Uzon Caldera is located within the Eastern Volcanic Zone of the Kamchatka Peninsula, 180 km north of the capital city Petropavlovsk-Kamchatsky and 25 km inland from the Pacific Ocean (Fig. 2). Pre-caldera volcanic history extends back into the middle Pleistocene, 225-370 thousand years ago (ky), where a shield volcano underwent a transformation as a large stratovolcano began to form on its western side (Karpov 1998). This period of volcanic activity was dominated by basaltic and minor andesitic lava flows and tuffs (Karpov 1995). Between 175 ky and 225 ky, a series of explosive eruptions produced the Uzon Caldera (Karpov 1998). After the Uzon formed, the caldera underwent further volcanic activity and alteration to produce its present form. Post-caldera activity included the formation of a large lake that lasted for 50 to 70 ky, a dacitic resurgent dome formation (Mt. Belaya) 10-12 ky, felsic lacustrine tuffs intruded by dacite 12 ky, and an andesitic maar formation (Lake Dalneye) in the early Holocene (Karpov 1998; Karpov and Naboko 1990).

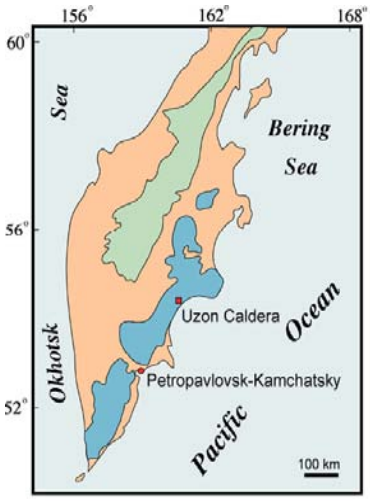

Figure 2. Map of the Kamchatka Penninsula, Russia. Crowe and Karpov 2004.

Glacial activity also molded the landscape of the caldera, as ice sheets 100-150 m thick descended the slopes of the caldera walls (Karpov 1998).

Currently, the Uzon Caldera contains five main hydrothermal fields: Eastern, Central, North, West, and Orange (Fig. 3), collectively comprising hundreds of geothermal features located along a main fault trending WNW and subsidiary faults trending NNE. Ring fractures are located along the base of the caldera walls, but the majority of the hydrothermal activity is along the main fault.

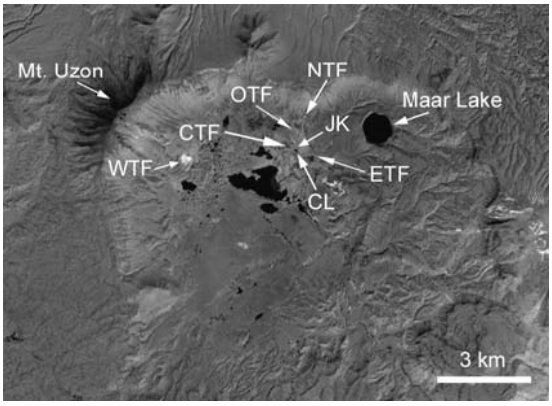

Figure 3. Satellite photo of the Uzon Caldera. The caldera contains five hydrothermal fields: North Thermal Field (NTF), Orange Thermal Field (OTF), Central Thermal Field (CTF), West Thermal Field (WTF), and Eastern Thermal Field (ETF). Jenn's Pools (JK) flows into Chloride Lake (CL). Crowe and Karpov 2004.

Hydrothermal activity is driven by a magma chamber, approximately 2 km from the surface, with the main magma body 10 km below the caldera floor. Colluvial deposition from the caldera walls alluvial deposits cover most of the geothermal regions

Field site

The focus of this study was two high temperature, disaerboic, reducing springs (based on Eh; Table 1.) called Vent 1 and Vent 2 of Jenn's Pools (Fig. 4). Vent 1 and Vent 2 are 13 m apart and have outflows that drain into Winding Stream which, in turn, inflows into Chloride Lake located in the Central Thermal Field (see Fig. 2). Vent 1 is a sulfate type spring, and Vent 2 is a mixed sulfate- chloride-bicarbonate spring. The source of spring fluid is mostly meteoric water, with average $\delta^{18}O$ and δD values of –14.47 ‰ and –111.22 ‰ for Vent 1, and –13.69 ‰ and –108.88 ‰ for Vent 2, respectively (Jones et al. 2004). Gases emitted from Vent 1 and Vent 2 have CH4/CO2 values of 9.68×10^{-3} and 1.98×10^{-2}, respectively (Romanek et al. 2004). Additional gases emitted include water vapor, hydrogen, hydrogen sulfide, and ammonia (unpublished data, Romanek 2004).

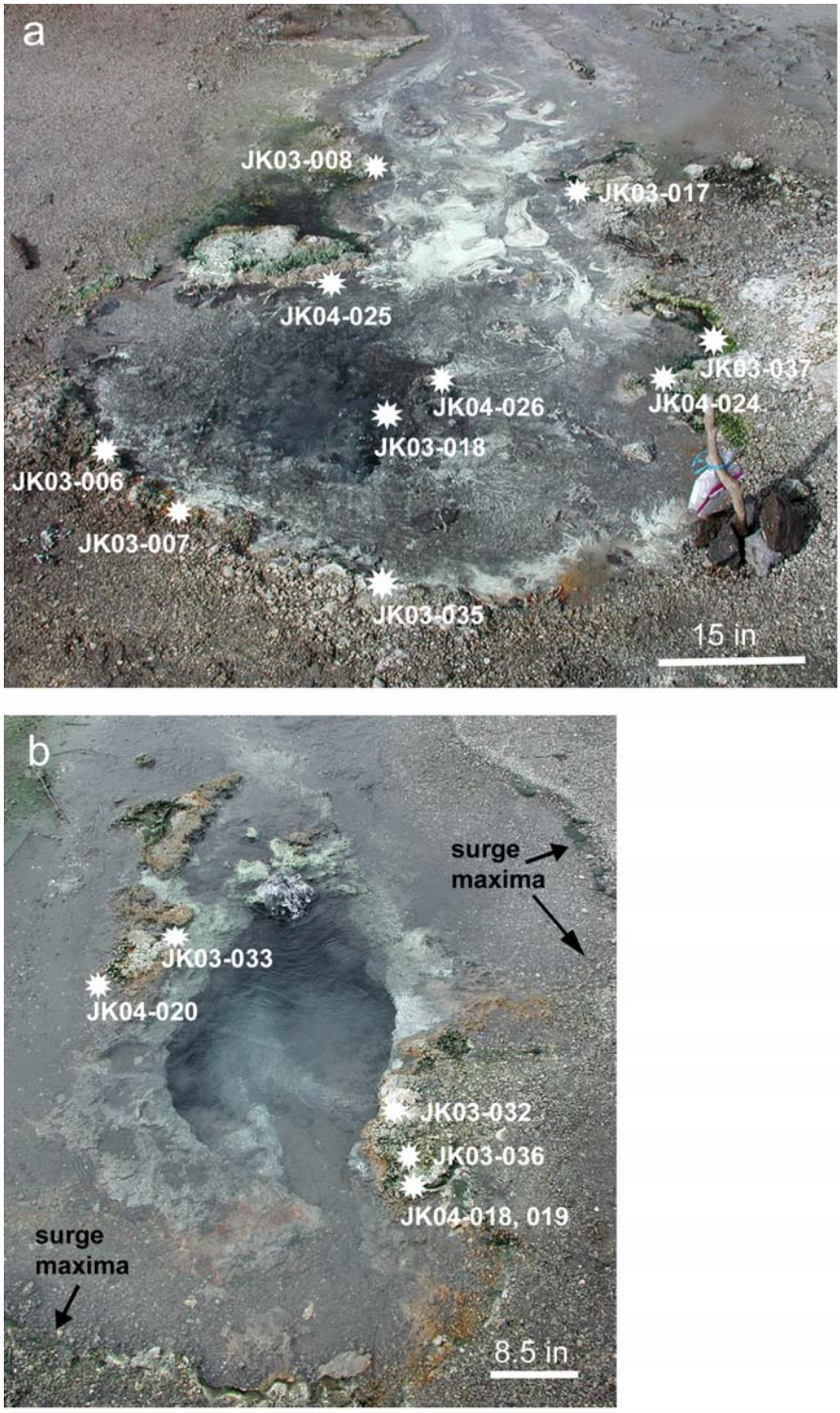

Figure 4. Photographs of Jenn's Pools within Winding Stream. Sample site for Vent 1 (a), and Vent 2 (b) are shown. Sample locations are labeled by the sample number. Surge maxima for Vent 2 is shown by the outer rim surrounding the vent (arrows), and surge minimum is confined within the vent.

CHAPTER 2

METHODS AND MATERIALS

Vent 1 is a non-surging spring with no rim overflow whereas Vent 2 is a surging spring with a mean surge of 5.4 minutes in which high surge overflows the vent rim. Vent 1 and Vent 2 sinters formed within the splash zone of the springs, all of which formed above the air/water interface, sinters are attached to a dark host rock which was once andesine (Hollingsworth et al. 2004). Vent 1 sinters are not submerged by spring fluids, whereas for Vent 2, some of the sinters forming directly along the edge of the vent are submerged by spring fluids during surge maxima. The majority of the siliceous sinter deposits were composed of spicules up to a few millimeters in length that were oriented vertically. Green microbial mats were commonly associated with most sinters, but tan and pink mats were also noted.

Field Work

Siliceous sinter was collected in August and September of 2003 and 2004 from Vent 1 and Vent 2 of Jenn's Pools (Fig. 4 and 5). Sinter samples with attached microbial mats were collected to determine the mineral phases present in the sinter, underlying rock, and within the mats, and also to identify any microbial-mineral relationships within the sinter and overlying microbial mats.

Surge rates of vent 1 and vent 2 were determined indirectly by the use of temperature loggers. Thermocouple sensors were placed between the vent edge and surge water level maxima. During high surge periods the thermocouple would be exposed to the high temperature spring fluids, whereas during low flow periods, the thermocouple would be exposed to lower

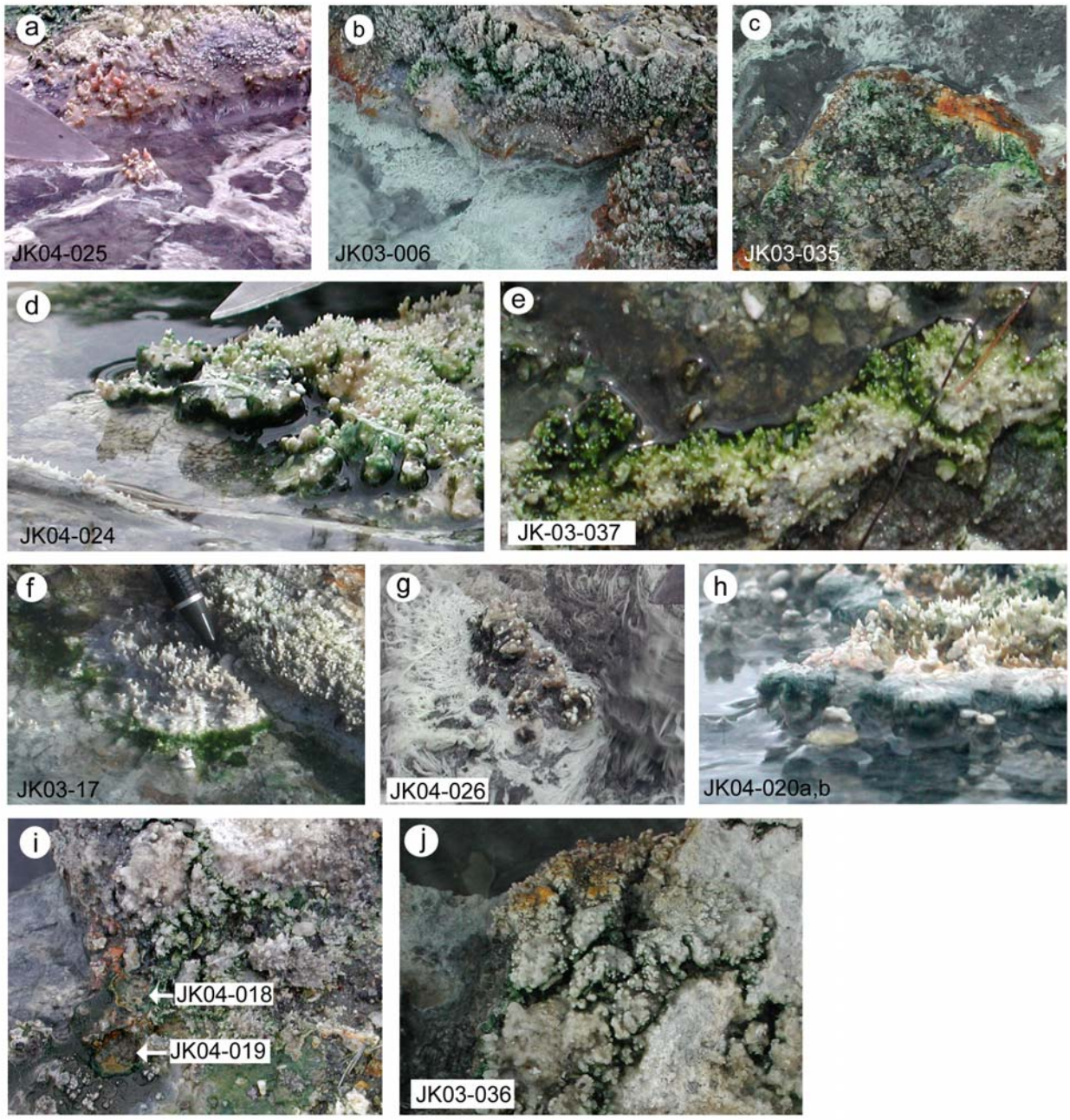

Figure 5. Close up images of samples collected from the field: Vent 1 (a-g) and Vent 2 (h-j). Knife blade and pencil shown for scale.

atmospheric temperatures. The time difference between high and low temperature readings indicated the surge rate of the springs.

In the field, spring fluid constituents were measured using colorimetric methods and a field spectrophotometer. Spring fluid was collected using a Teflon dipping cup and immediately transferred to vacutainers. The following tests were performed: total iron, ferrous iron, sulfate, phosphate, dissolved oxygen, nitrate, nitrite, and copper. Total soluble sulfide was measured using a CHEMetrics K-9507 kit (Methylene blue method), alkalinity was measured using a HACH AL-AP-MG-L (titration to pH 4.5 using phenolphthalein indicator), and arsenic was measured using a CHEMetrics 2822800 test kit. Biofilms, sinters, and underlying rock samples were collected using a rock hammer and knife. Some specimens were placed in fixative solution (described below) for later work on electron microscopes. Samples collected for bulk mineral analysis were not chemically fixed but stored in plastic containers and bags for later analysis.

Laboratory work

Bulk mineral analysis of the sinters and underlying rock was conducted using X-Ray Diffraction (Scintag® XDS2000) with a Co Kα radiation target source. Samples were ground into a fine powder using a mortar and pestle and then mounted onto a zero background quartz plate using an acetone slurry. Initial scan rates were conducted using 2º/4º scattering slits, 0.5º/0.2º receiving slits, a 0.6 second counting time at a continuous scanning rate of 2.0º/min. Additional analyses were conducted on samples that required a higher signal-to-noise ratio. Experimental parameters for these samples included a step count of 0.01° with a 10-15 second count time.

Thermogravimetric Analysis (Hi-Res® TGA 2950) was used in identify mineral phases, especially in the kaolin group minerals, and also to measure the abundance of mineral phases present within the sample. Approximately, 14 mg of sample was ground into a fine powder using a mortar and pestle. Each sample was equilibrated at 30° C, with a scan ramp parameter of 50°

C/min (5° C resolution) from 30° C to 700° C. Standards of kaolinite, elemental sulfur, and gypsum were found to undergo dramatic weight loss at 466° C, 188° C, and 127° C, respectively. Opals lose most trapped and absorbed water from 105º C to 115º C (Jones and Renaut 2004), and dehydroxylate between 215º C to 350º C (slightly varies with scan parameters; Brown et al. 2002).

Electron Microprobe Analysis (EMPA) was conducted using a JEOL® 8600 Superprobe with an accelerating voltage of 15 kV. Thin sections were made from samples JK03-006, JK03-007, and JK03-032a by submerging them in epoxy resin placed in a vacutainer. The vacuum forced epoxy to infiltrate the samples quickly. When the vacuum was released samples were then placed in a fume hood at ambient temperature until the resin hardened. Millimeter-sized sections were cut and glued onto glass slides, and then grounded using silicon carbide 320 micron grit sandpaper into thin sections. After the sections were thinned, they were progressively polished using 600 μm and 1000 μm diamond grit. Before viewing the thin section on a light microscope, the surfaces of the sections were cleaned by blowing pressurized air across the surface to remove any dust that may have settled onto the surface. Carbon coated thin sections were mounted into the microprobe for elemental analysis using a energy dispersive spectrometer at 15 keV with a beam accelerating voltage of 15 nA. Elemental maps of iron, sulfur, and aluminum were acquired using wavelength dispersive spectroscopy (WDS) with a dwell time of 3 μs/pixel.

Energy Dispersive Spectroscopy (EDS) was used in conjunction with Scanning Electron Microscopy (SEM; Leo® Field Emission 982 SEM) operating at 20-25 keV to analyze regions of interest, including mineral coatings on microbial cells, microbe-like structures, crystal habits, and their spatial relationships. Parameters for EDS are noted below when discussing techniques

for SEM.

The SEM was used to analyze samples at 5 kV for secondary electron imaging (SEI) up to 25 kV for backscatter electron imaging (BSE) of crystals, microbial coatings, and other regions of interest.

Year 2003 and 2004 samples underwent different chemical fixative techniques to examine if one method was better at preserving the mineral-microbe interface. In 2003, samples were immediately submerged in 2% glutaraldehyde (to fix proteins) and stored at ambient temperature until the samples were returned to the lab (maximum exposure period was two weeks in glutaraldehyde). Samples were subsequently transferred into phosphate buffered saline (PBS) for three washes lasting 10 minutes each. This buffer is an isotonic solution detaches cells from sediment surfaces (Bennett and Engel 2004). Samples were then transferred into secondary fixative solution to fix lipid molecules, osmium buffer solution (1 part distilled water, 1 part osmium tetraoxide, and 2 parts PBS), and stored at 4 ºC overnight. The samples were then washed 3 times in distilled water for 15 minutes. A stepwise dehydration series followed, using ethanol/water concentrations at 30%, 50%, 70%, 85%, 95%, and 2 times at 100% ethanol for 30 minute intervals. The samples were critical point dried in which the samples were submerged in 100 % ethanol within a bomb. The ethanol was displaced with liquid carbon dioxide, and then the temperature of the vessel was raised causing an increase in pressure within in the vessel until the critical point of the liquid carbon dioxide is reached. The vapor was then released while the temperatures is maintained until the vessel is at atmospheric pressure. Samples were then removed, mounted onto aluminum stubs, and then carbon coated to enable EDS analysis.

Samples collected during the 2004 season underwent a slightly modified fixation procedure (Bennett and Engel, 2004). Samples collected in the field were washed 3 times for 10

minutes in 0.05 M Cacodylate buffer. The samples were then transferred into a mixture of 2% glutaraldehyde, 50 mM lysine, and 0.05 M Cacodylate for 90 minutes. Samples were then stored in 1% glutaraldehyde in Cacodylate buffer at air temperature until the samples were brought back to the lab. Samples were subject to the same ethanol dehydration series as above but for 20 minutes each, and then chemically dried in hexamethyldisilazane (HMDS) two times for 20 minute intervals. Samples were loosely covered and left to air dry overnight, mounted on aluminum stubs, and carbon coated for viewing on the SEM.

The sampling strategy for TEM analysis was based on acquiring representative pieces of mats around the sinter. Small pieces of microbial mat were removed from the sinter sample. Sinter and attached microbial mat were also removed. The samples were placed in containers and fixed and dehydrated as stated above. The final preparation proceeded by infiltrating samples with propylene oxide for 45 minutes. They were then transferred to a 2:1 mixture and then a 1:2 mixture of propylene oxide to Epon (resin) for 1.25 hours each. Samples were transferred into 100% Epon for 1.25 hours and then again into fresh Epon overnight. A final step involved again transferring into fresh Epon, at which point the samples were held at 60ºC until the Epon hardened.

Fixed samples were cut into section using an ultramicrotome TEM analysis. Sectioned samples were mounted on formvar coated copper grids and analyzed for morphological properties using a JEOL 100 CX II. Samples were analyzed unstained to prevent the formation of secondary staining artifacts that have electron densities similar to inorganic phases of interest. After initial viewings, those samples that contained little to no evidence of mineralization underwent a staining with uranyl acetate and lead citrate to enhance cellular membranes for imaging.

Samples that contained abundant mineralization were analyzed on a Philips (FEI) CM300 FEG TEM with scanning transmission electron microscopy (STEM) and Gatan Imaging Filter (GIF) to conduct EDS, selected area electron diffraction (SAED), and electron energy loss spectroscopy (EELS), and Philips 420 TEM for EDS and SAED. Fifty angstroms of carbon was coated onto sections to stabilize the samples under the electron beam. Particles undergoing SAED were centered under the beam and imaged at various exposure times to obtain information from outer rings of the diffraction image. Elemental maps were conducted using EELS in which the zero loss peak image (elastically scattered electrons) and plasmon images (the oscillation of electrons on the surface of the sample) were taken to align the beam and adjust parameters to obtain the most accurate elemental map. Custom elemental maps were then imaged at various exposures to obtain the most precise image of the distribution of the element of interest.

CHAPTER 3

RESULTS

Spring fluids for Vent 1 and Vent 2 were generally similar, with both being high temperature (~80°C), acidic to neutral pH (pH 5.3-6), reducing (Eh =-240 to -100 mV), and undersaturated with respect to dissolved oxygen. Some distinct differences do occur between the two vents. These include greater concentrations of nitrate, alkalinity, and total arsenic in Vent 1 (Table 1). The only notable temporal change in spring water composition was the decline in total silica from year 2003 to year 2004. Total silica values were lowered from 130 ppm to 77 ppm, and 139 ppm to 88 ppm for Vents 1 and 2 respectively (unpublished data Crowe 2004). These total silica values are considered undersaturated in a spring at 75° C to 80° C. The solubility of amorphous silica at 75° C is 269 ppm, where solubility will increase with increasing temperature (Rimstidt and Cole 1983).

Mineralogy

All of the sinters collected were thin (millimeters thick), highly laminated, and mainly composed of spicules up to 5 mm in length. The sinter mineralogy was dominated by opal-A, which is identified in XRD patterns by the broad semi-coherent peak centered around 4.04 Å (26° 2Θ; Fig. 6). An aluminum WDS map revealed that these sinters are highly laminated with Al (Fig. 7 – sample JK03-007). Opal-CT was also observed in many of the sinters, as a small coherent XRD peak at 4.04 Å, having a corresponding shoulder with a slightly larger d-spacing/smaller 2Θ. Many of the sinter XRD patterns also contained a small peak at 2.5 Å (~ 42°

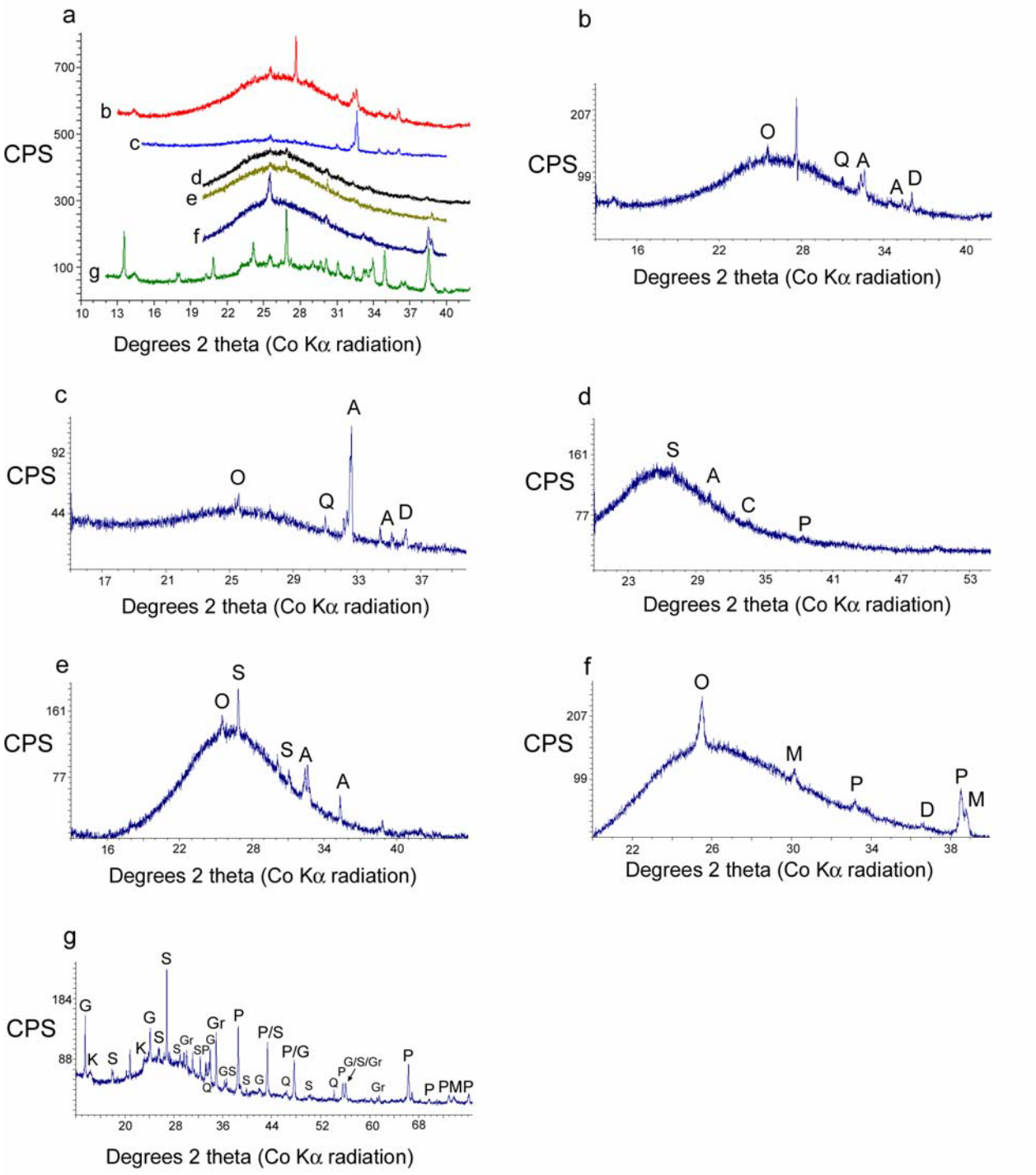

Figure 6. XRD of siliceous sinter. (a) Diffractogram of all sinters from Vent 1 (b-d) and Vent 2 (e-g). (b) JK03-006, (c) JK03-007, d) JK03-008, (e) JK03-032a, (f) JK03-032b, and (g) JK03-033. CPS- counts per second; O- opal-A/opal-CT; Q- quartz; A- andesine; D- dolomite; S- sulfur; C- calcite; P- pyrite; M- marcasite; G- gypsum; H-halloysite; Gr- greigite

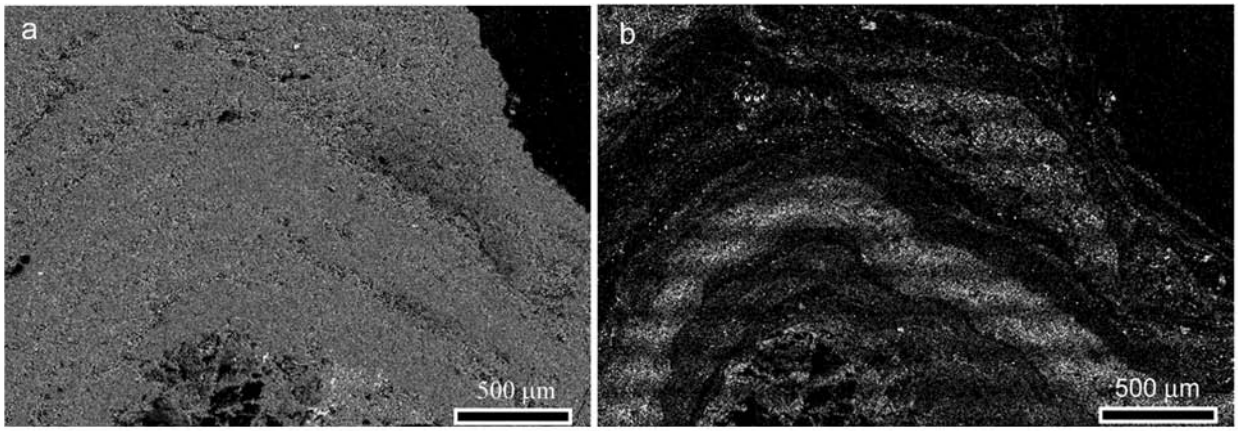

Figure 7. Secondary electron image (a) and Al map (b) of sinter from JK03-007. Laminations noted in (a) correspond to laminations noted in (b).

2Θ), which was indicative of opal-CT. Other minerals identified through XRD within the sinters included quartz, andesine, elemental sulfur, kaolin group minerals, calcite, dolomite, gypsum, pyrite, marcasite, greigite, magnetite, and hematite (Table 2). TGA analysis shows weight loss at temperatures of 459°C to 483 °C, which indicated a kaolin group mineral found in some of the sinter samples (Table 3). Other mineral phases found through TGA, elemental sulfur and gypsum (Appendix 2), were also identified in the corresponding XRD diffractograms.

Elemental analysis was conducted on chemically preserved samples through SEM/EDS. Samples collected in 2004 using a modified fixation procedure were dehydrated with HMDS which is gentler on the microbial mats attachment sites and EPS then critical point drying (Bennett 2004), conducted on 2003 samples. The 2004 technique does not react well with sulfate as sulfates dissolve quickly in the fixative (Bennett 2004) although there were no noticeable effect. Table 4 lists mineral phases in the sinter whose compositions were found through EDS. Eight out of the fifteen mineral phases identified are known to be produced through biologically induced and/or controlled mineralization (Weiner and Dove 2003). Pyrite was found in various habits, such as cubes, octahedron, and framboids (Figure 8 a-c). Silica

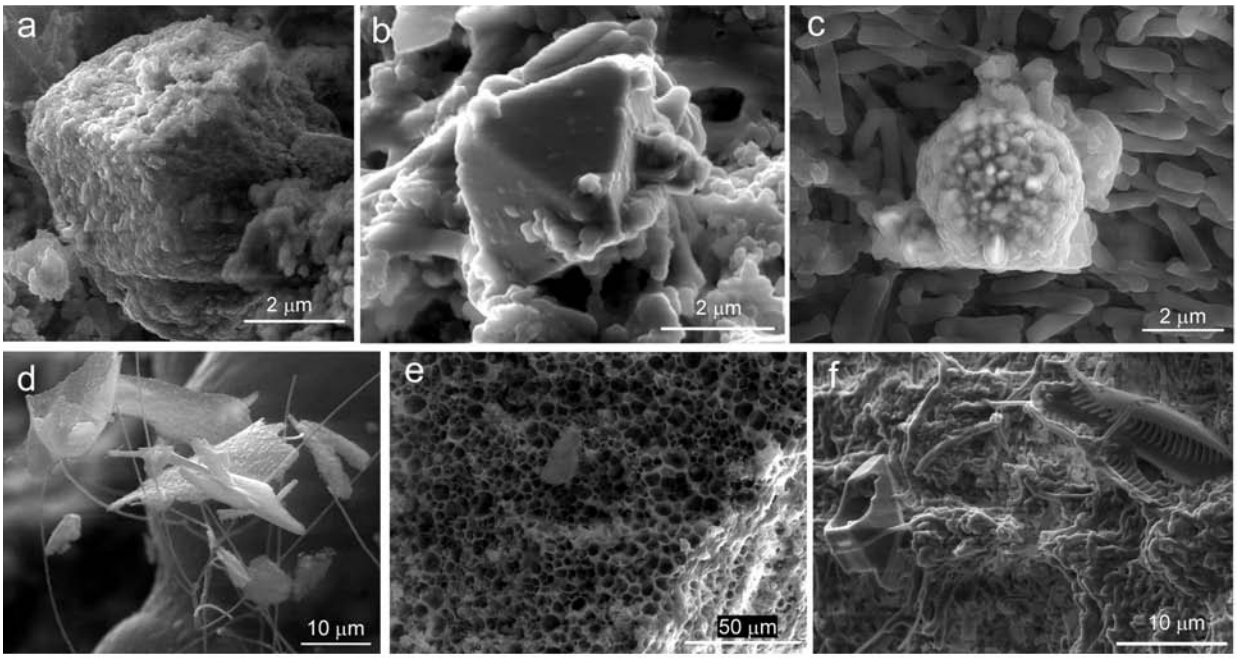

Figure 8. Mineralogy of sinter from Vent 1 analyzed through SEM and EDS analysis. (a) Cuboidal pyrite covered in silica, (b) pyrite surfaces with attached rod shaped silica phases, (c) famboidal pyrite on the top of a microbial mat at a spicule tip, (d) iron oxide/hydroxide crusts attached to ESP, (e) carbonate surrounded by microbial matter and near a diatom test, and (f) honeycomb opal-A surface texture.

overgrowths were found to completely cover pyrite surfaces (Fig. 8a), and also partially cover pyrite surfaces as siliceous rods (Fig. 8b). Framboidal pyrite appears to be encompassed in a thin coating residing on top of a microbial mat at a spicule tip (Fig. 8c). Iron oxide/hydroxide crusts attached to filaments, believed to be exopolymeric substances (EPS; Figure 8d). The sinters occasionally feature opal-A honeycomb textures (Fig. 8e) composed of micron sized depressions. Carbonate occurs surrounded by organic material (Fig. 8f).

The host rock of Vent 1 was a highly clay altered, whereas the host rock for Vent 2 was dominated by opal-A (Fig. 9). Kaolinite (Fig. 10a) was the dominant clay mineral in Vent 1, however in some instances halloysite was found (Fig. 10b, c). Halloysite was found as a white precipitate often ponded as a sediment in constant contact with spring fluids (e.g., sample JK03-035). Pyrite occurred commonly in the form of cubes and framboids, residing in veins, and

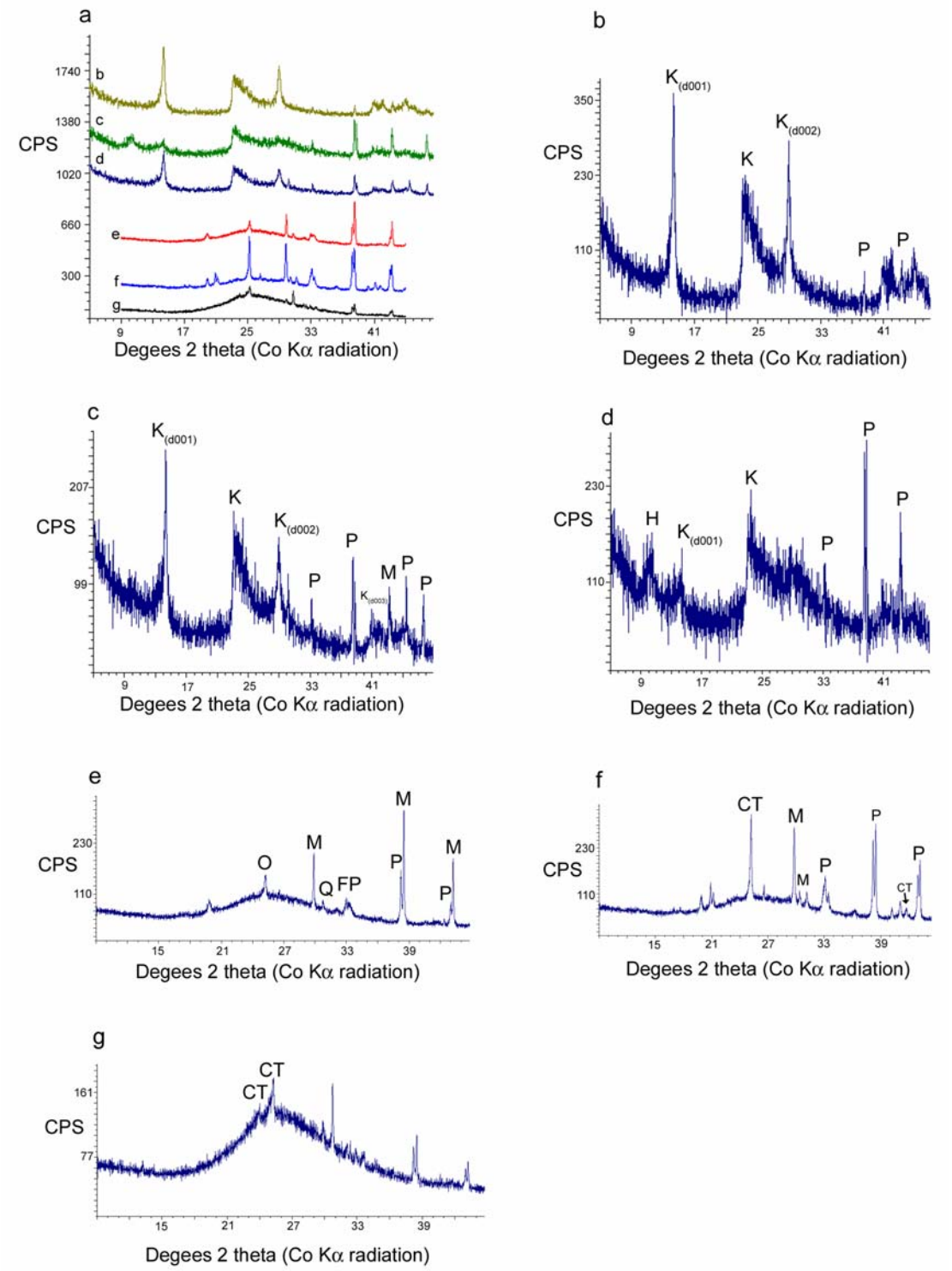

Figure 9. XRD of underlying rock. (a) Diffractogram of all underlying rocks from Vent 1 (b-d) and Vent 2 (e-g). (b) JK03-006, (c) JK03-007, d) JK03-008, (e) JK03-032a, (f) JK03-032b, and (g) JK03-033. CPS- counts per second; K- poorly ordered kaolinite; P- pyrite; M- marcasite; O- opal-A; CT- opal-CT; and Q- quartz.

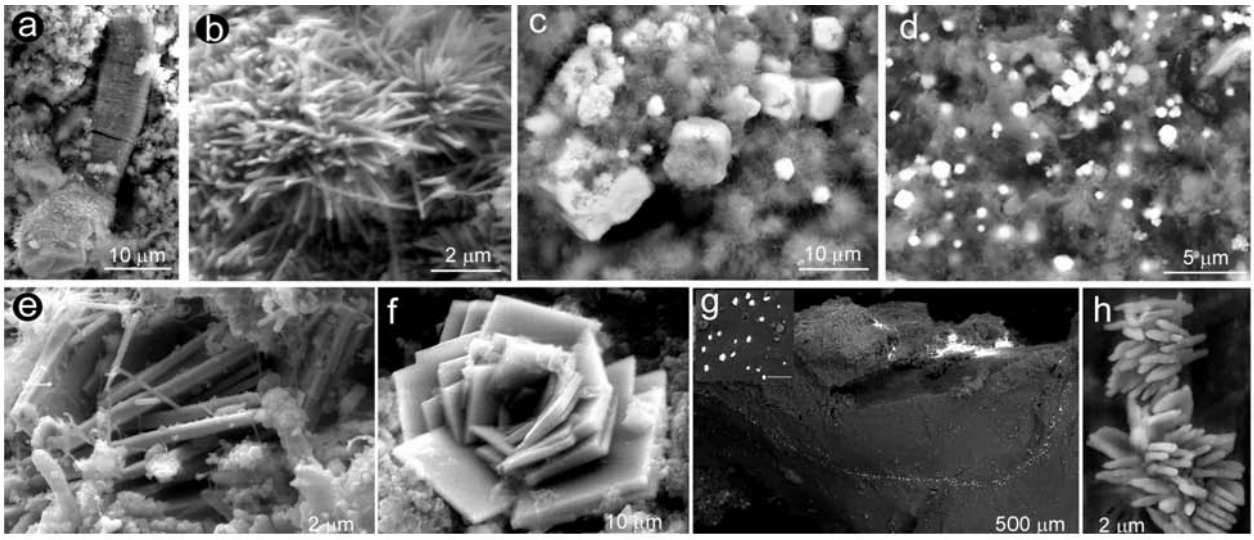

Figure 10. Mineralogy of the underlying rock examined through SEM/EDS analysis. (a) Stacked kaolinite crystals, (b) halloysite tubes, (c) pyrite cubes surrounded by halloysite, (d) disseminated pyrite amongst halloysite, (e) barite laths, (f) barite rose, (g) cinnabar vein running through sample; scale bar on close up of grains 20 μm, and (h) rod-shaped minamiite (?) crystals.

as disseminated grains throughout the rock (Fig. 10d). Lath-shaped barite crystals (Fig. 10e) and occasional rose habits (Fig.10f) were also found throughout the rocks. Cinnabar was found forming as a vein running through a large portion of the substrate (Fig. 10g), and an alunite group mineral with an EDS spectrum consistent with minamiite was found as isolated rod shaped clusters (Fig. 10h). Jarosite (another alunite group mineral) was found with rock sample JK03-018, which lined the edge of Vent 1. Table 5 lists additional mineral phases found in the rock underneath the sinter, which were identified through a combination of EDS and XRD. Seven out of sixteen of these mineral phases are of known biological induced and/or controlled mineralization (Weiner and Dove 2003).

A thin section of rock substrate from Vent 1 (JK03-007), analyzed by backscatter electron imaging and EDS, revealed a nodule surrounded by pyrite embedded in kaolinite (Fig.11). A cross-section of the nodule revealed it was separated into quadrants by pyrite with internal laminations of anatase.

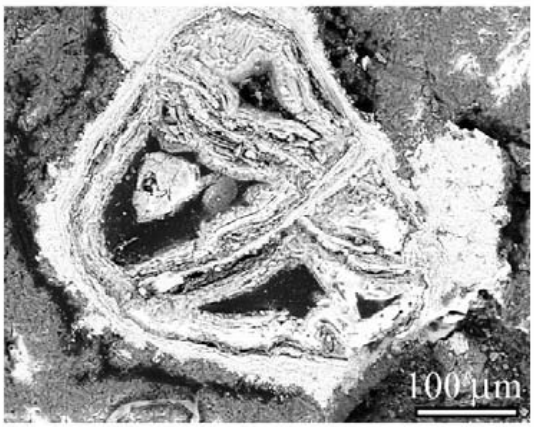

Figure 11. Combined secondary and backscatter electron image of pyrite and anatase nodule within kaolinite found in JK03-007. Bright regions represents pyrite (not pyrite sections nodule into quadrants), and gray laminations within the nodule represent anatase.

Microbe/Mineral interactions

The microbe-mineral relationship observed through SEM showed a relationship whereby organisms were commonly associated with iron-bearing mineral phases. Microorganisms were found attached to pyrite through the extension of EPS (Fig. 12a), in direct contact with iron-oxide/hydroxide spheres (Fig. 12b), and iron coated EPS (Fig 12c). Rod shaped structures (sometime covered with silica) were found embedded in sinter (Fig. 12d). Titanium-bearing mineral phases and barite were commonly found in the sinters but they were rarely in contact with microorganisms (Fig. 12e). Given the sinters were covered by microbial mats, extensive EPS networks were often evident along the surface of most of the samples (Fig. 12b, f) and were attached to a variety of mineral phases (Fig. 12g, h). The most common microbial-like morphologies noted in the sinters from Jenn's Pools were rod-shaped structures around 2 µm in length and segmented filaments up to 20 µm in length (Fig. 12b, i). In addition to these prokaryotic forms, diatoms were also abundant on samples from the vent rims. Diatoms are typically 20 to 30 µm long with striae radiating towards the central area, and lobed ends resembling *Pinnularia* species (based on morphology and size of the diatoms;

www.umich.edu/~phytolab/GreatLakesDiatomHomePage/Pinnularia). Diatom test imprints within the opal-A substrate (Fig. 12j) were common in addition to complete diatom frustules (Fig. 12k). One sample collected from the outer northwest rim of Vent 2 contained numerous spores coating one side of spicules. Most of the spores were 1 μm to 2 μm in diameter, some of which were split or in some instances only the spore coat remained (Fig. 12l).

Unmineralized forms resembling fungal cells were found through TEM analysis of the mats (Fig. 13).

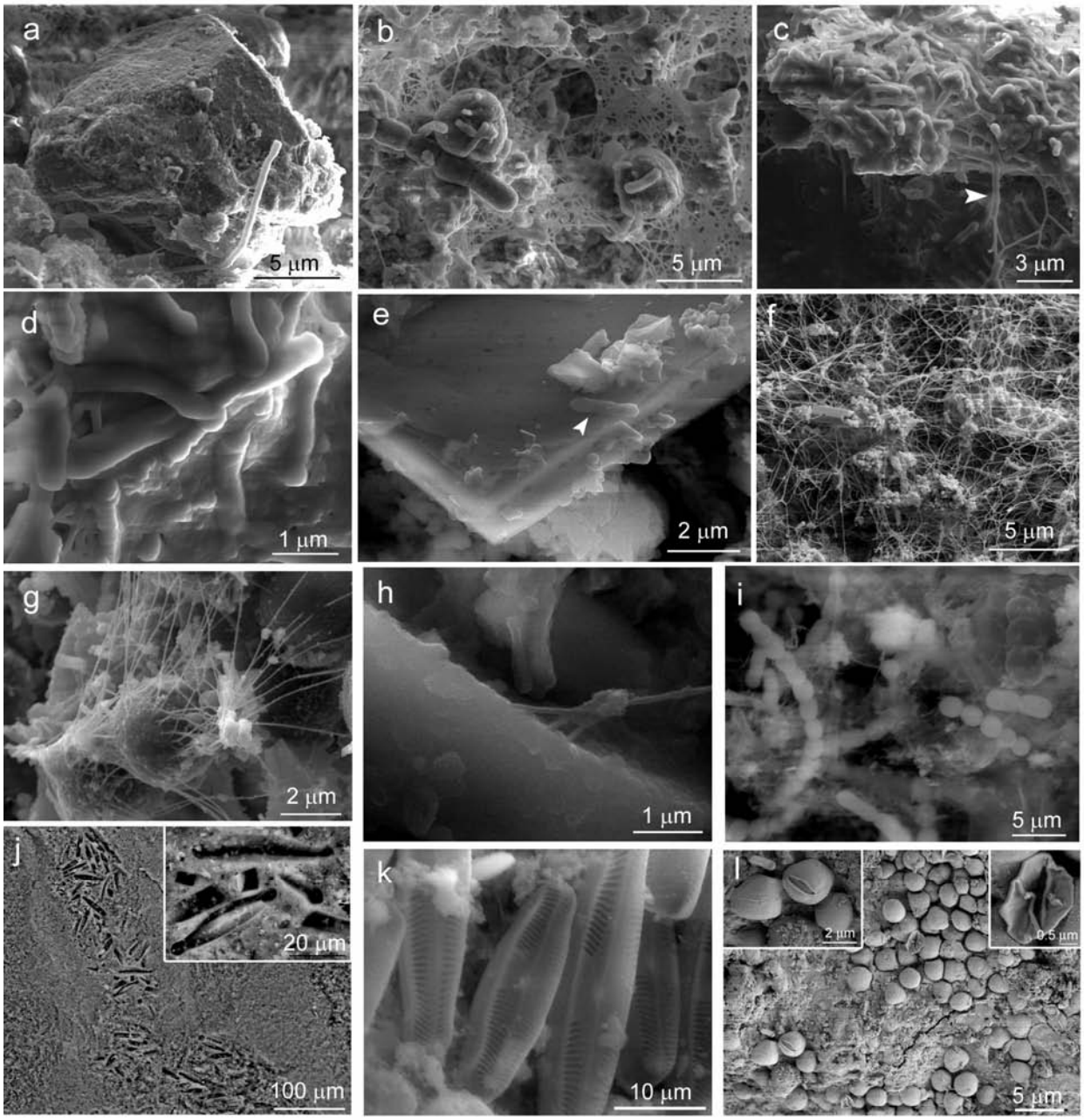

Figure 12. Microbe-Mineral relationships found through SEM/EDS analysis. (a) Cuboidal pyrite with attached filament and hollow tubes attached to lower end of the pyite, (b) extensive EPS network with segmented/chained and rod-shaped structures attached and/or in contact with iron oxide or silica spheres, (c) iron coated EPS (white arrow) draping from silica dominated substratum, (d) close up of substratum in (c) with silica covered rods, (e) barite with microbe-like structure along the crystal edge, (f) extensive EPS network along sinter surface, (g) EPS attached to iron-bearing sphere, (h) EPS attachment to silica phase, (i) segmented filament, (j) diatom imprints within sinter, (k) *Pinnularia?* diatom frustules, and (l) spore? coated spicule.

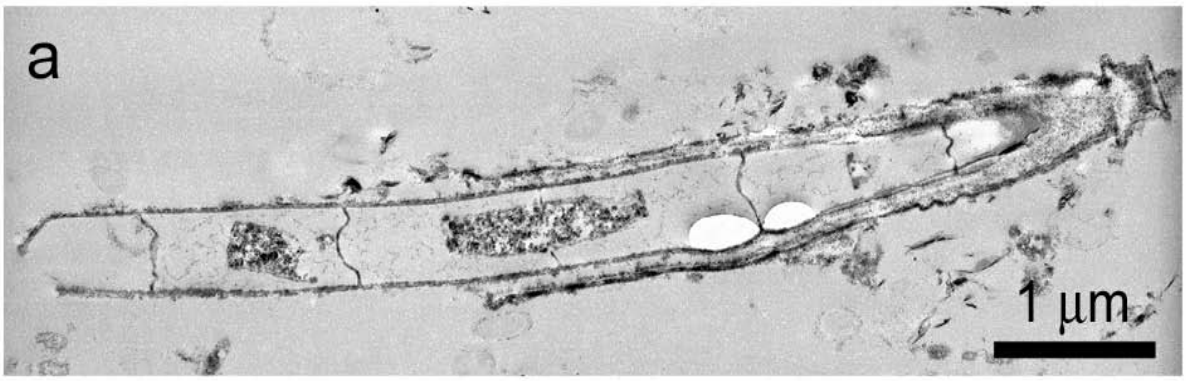

Figure 13. Possible fungal form found in JK04-019-c2. Note cell septa running across the cell.

Biomineralization

Silicified tubes were also commonly found. A common remnant of cellular entombment is an extracellular silica mold (Fig. 14). Some of the silicified tubes were segmented (Fig. 14a), while others were long and linear (Fig. 14c). Both tube morphologies resembled structures noted in figure 12. All of the silicified tubes have rough exteriors and smooth interiors, and the degree of silica accumulation varied as some tubes were thickly mineralized (Fig. 14b) while others were not (Fig. 14d).

Evidence of cellular preservation within the underlying rock was observed in thin sections of Vent 1 sinters (Fig. 15). The filamentous structure within JK03-007 (Fig. 15a) lies within the kaolinite dominant region and in the opal-A dominant region for JK03-032a (Fig. 15b). Focusing and defocusing the microscope on the structures revealed the filaments were embedded within the rock matrix and not merely residing on the surface. When these structures were examined using the electron microprobe, they volatilized under the electron beam suggesting they were probably organic in nature. A curved segmented filamentous structure found in Vent 1 (Fig. 16a -JK03-007), was embedded in kaolinite. A WDS map revealed each segment was composed of sulfur (Fig. 16b). EDS analysis of the segments showed minor amounts of iron were also present.

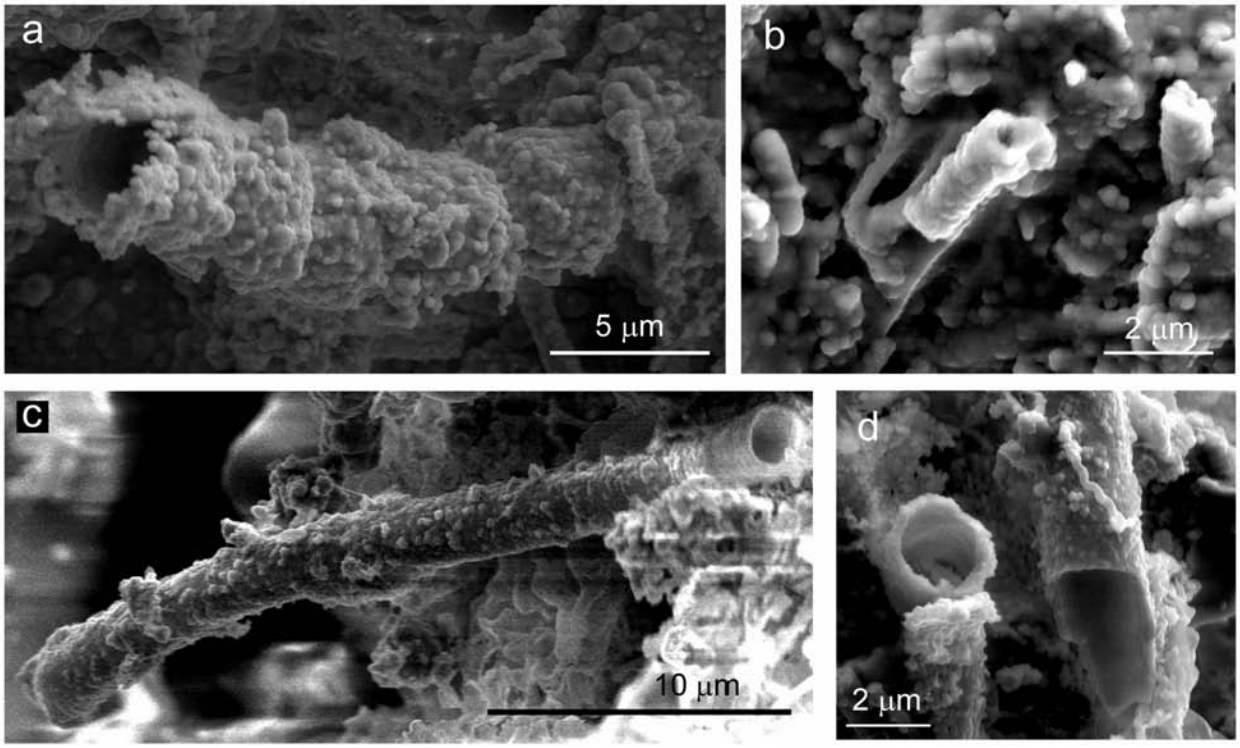

Figure 14. Silicified tubes with smooth interiors and rough exteriors. (a) Segmented tube attached to the substrate, (b) thickly mineralized tube, (c) long linear tube, and (d) broken thinly silicified tube.

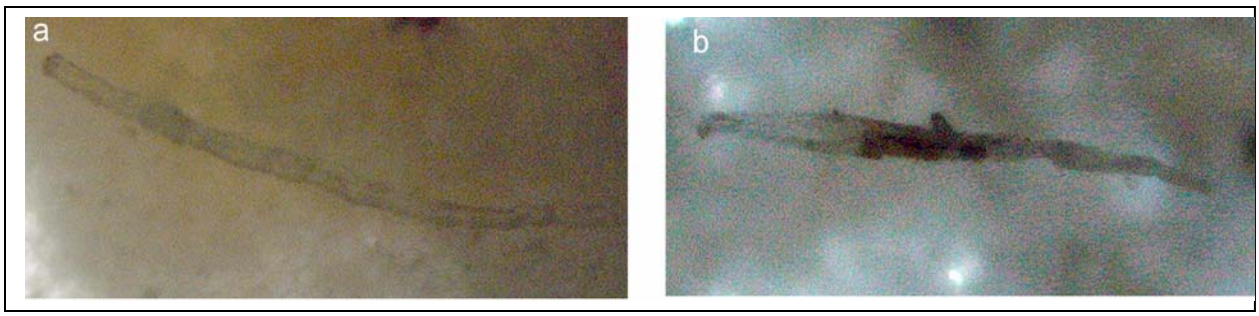

Figure 15. Filamentous structures resembling bacteria embedded in kaolinite dominated region of JK03-007 (a) and opal-A dominated region of JK03-032a (b). Each filament is approximately 200 μm long.

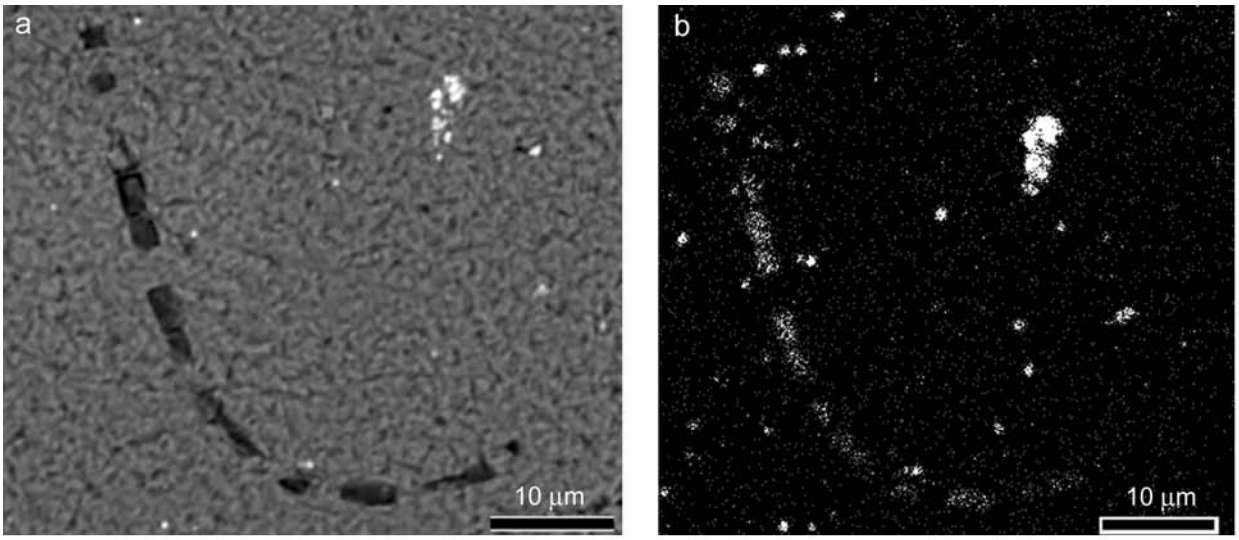

Figure 16. Combined secondary and backscatter electron image (a) and S map (b) of segmented filament from JK03-007. Bright spheres around segments are probably pyrite framboids within the kaolinite matrix.

Extracellular mineralization was prominently found in the form of opal-A spheres (Fig. 17) through EDS and HRTEM analysis. TEM/EDS analysis indicated iron maybe present in some of the samples but the Fe Kα peak overlapped with the escape peak for copper (from the copper grids).

Mats attached to sinters on the northwest rim of Vent 2 were divided into three sections (sample JK04-019; Table 6). The section closest to the sinter (JK04-019-a1) contained the most

heavily mineralized cells with multiple layers of opal-A spheres surrounding most cells (Fig. 17a-c). Most mineralization takes place away from the cell wall on the surface of the EPS surrounding the cells. Occasionally, the cell walls were thinly mineralized with smaller opal-A spheres than those away from the cell but only when the EPS was mineralized (Fig. 17b). In addition to silicified cells, hollow silicified structures were found in the shape and size of cells in the region (Fig. 17a, c). Mineralization primarily takes place symmetrically around the cells. The silicified crusts become thinner and cells are less mineralized farther into mat (Table 6). Cocci cells were the most common morphology in all samples, however segmented and/or chains of microbial forms become more abundant in some areas.

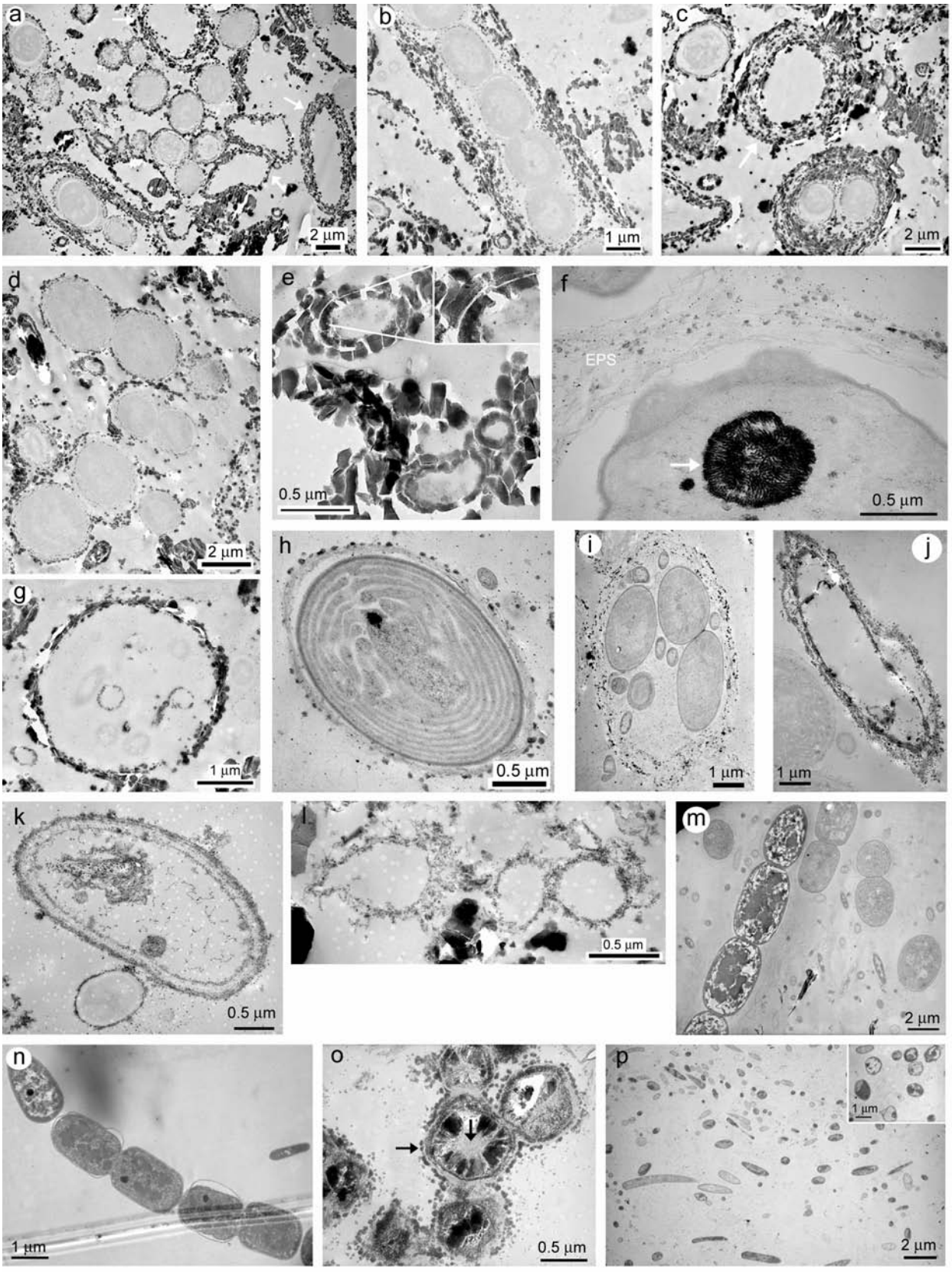
a
2 µm
b
1 µm
c
2 µm
d
2 µm
e
0.5 µm
f
EPS
0.5 µm
g
1 µm
h
0.5 µm
i
1 µm
j
1 µm
k
0.5 µm
l
0.5 µm
m
2 µm
n
1 µm
o
0.5 µm
p
1 µm
2 µm

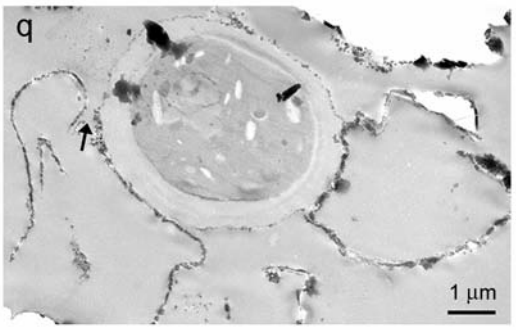

Figure 17. Transmission electron micrographs of mat samples collected from sinter deposits from Vent 2 (a-l), and Vent 1 (m-q). (a) Extracellular silicification of cells and silicified molds (arrows; JK04-019-a1), (b) Silicified EPS surrounding cell and initial silicification of cell wall of segmented prokaryote (JK04-019-a1), (c) heaviliy silicified cells and extracellular silicified mold (arrow) (JK04-019-a1), (d) thinly mineralized cocci cells with intracellular membranes (JK04-019-a2), (e) spherical and rod- shaped structures composed of blocky particles (JK04-019-a2), (f) polyphosphate granule within cell (arrow), and strands of EPS surrounding cell (JK04-020), (g) silicified mold with smaller mineralized and unmineralized cells within mold (JK04-019-a2), (h) intense intracellular membranes of lightly mineralized cell (JK04-019-b1), (i) cocci cells surrounded in lightly mineralized EPS (JK04-019-b1), (j) silica mineralized rod-shaped cell with internal segment next to unmineralized cocci cells in the lower left of the micrograph (JK04-019-c1), (k) cell with silica on EPS surface; smaller cocci cell causing indentation in larger cell (JK04-019-c2), (l), olds composed of strands of nanometer sized particles (JK03-036), (m) unmineralized cells; smaller cells have intracellular membranes (JK04-024-a), (n) unmineralized chains of cells that appear segmented (JK04-024-a), (o) cell-sized cocci with outer spheres and center of cells composed of ferrihydrite (arrows; also see Fig. 18); darker structures in interior of cocci composed of pyrite (JK04-024-b), (p) unmineralized microbial mat (JK04-025), and (q) large cell with silica around cell and silicified strands extending from the cell some of which appear detached (arrow; JK03-037a).

Mat material sectioned from the same region as above but further within the mat (JK04-019-a2) are also mostly mineralized but to a lesser degree than those closer to the sinter. The majority of cells are surrounded by either a single or double layer of opal-A spheres (Fig. 17d). In addition to mineralization via opal-A spheres, cells were occasionally mineralized by blocky structures of unknown composition (Fig. 17e). More deeply into the mat (JK04-019-a3), mineralization is minimal, as most cells are not mineralized, with no evidence of silicified tubes or cells. Both samples JK04-019-a2 and JK04-019-a3 contained small mineralized and

unmineralized cells within the silicified hollow tubes (Fig. 17g).

Another mat sample collected adjacent to the first but further from the sinter of Vent 2 (JK04-019b) varied slightly from JK04-019a. Most of the cells (~95%) for JK04-019-b1 contained intracellular membranes within the cytoplasm of the cell (Fig. 17h). These membranes resemble thylakoids (photosynthetic membranes used in photosynthesis) found in cyanobacterium *Synechococcus lividus* (Edwards and Gantt 1971). The intracellular membranes could also represent nonphotosynthetic membranes from other groups of microorganisms such as nitrifying bacteria. Similar sized and shaped cells in close proximity to one another were enclosed with EPS that was thinly mineralized (Fig. 17i). Most of the cells are not mineralized, but the occasional EPS around a cell contains partial or discontinuous mineralization. Most of the cells noted were cocci. Filamentous segmented cells are found rarely. Sampling farther into the microbial mat (JK04-019-b2) revealed forms similar in the above sample (JK04-019-b1).

A third mat sample was collected on the opposite side of JK03-019a (JK04-019c) to further evaluate sinter/mat heterogeneities. Sections from this sample differed from the others in that many of the cells are commonly bacillus (rod-shaped) and typically contain a single filament running the length of the cell (Fig. 17j). Some of the cocci cells present contained intracellular membranes. The cells were either lightly mineralized with silica or not mineralized, some within less than a micron from each other (Fig. 17j). This image reveals that either preferential mineralization was occurring or the unmineralized cell was new to the system and hasn't had a chance to become mineralized. If the cells in JK04-019-c12 were mineralized, then the mineral particles were generally smaller than JK04-019-c1 and located within and on the outside of the EPS surrounding the cell. Mineralization style further into the mat (JK04-019-c2) was the same as near the sinter (JK04-019-c1) however, more cells were mineralized (Fig. 17k).

Material from sample collected on the northeast side of Vent 2 rim, JK04-020, that loosened and fell into chemical fixative solution was almost completely unmineralized although there was the rare occurrence of mineralized tubes. Polyphosphate inclusions (likely used as a phosphate reservoir and energy source for intracellular prokaryote metabolism) were found within some of the cells (Fig. 17f). Many of the cells were segmented, some of which contain two or three concentric layers of intracellular membranes. The cells with intracellular membranes were morphologically different (i.e. suggesting a different microbial species), however, they did not show a difference in the degree of mineralization.

Another sample (JK03-036) analyzed from Vent 2 was analyzed from the northwest side of Vent 2. It contained a few mineralized tubes with no evidence of organic components. The extracellular tubes were composed of nano-sized spheres that extended outward from the tube (Fig. 17l).

Vent 1 mat samples were similar to Vent 2 except they were not as heavily mineralized, and Vent 1 samples contained iron-dominated microbial forms. Mats sectioned from the southwest side of Vent 1 were completely unmineralized with occasional cells having intracellular membranes (Fig. 16m; JK-04-024a). Most cells were cocci with some evidence of segmentation (Fig. 16m, JK04-024a) and chains of cells (Fig. 17n). Sections from further into the sinter/mat complex differed in that similar sized and shaped cell structures contained ferrihydrite spheres attached to the outside of the structure with ferrihydrite and pyrite within the spherical structures (mineralogy determined by SAED; Fig. 17o and Fig. 18). HRTEM images of the ferrihydrite spheres outside the cell revealed random nanocrystals with ~ 0.22 nm to 0.26 nm d-spacings, and 0.26 nm to 0.30 nm d-spacing of ferrihydrite within the structures (Fig.18). The 2.6 nm d-spacing is consistent with the (111) plane of 2-line ferrihydrite (Janney et al.

2000). These nanocrystals produced a diffuse SAED pattern which indicated the iron oxide spheres were highly disordered. HRTEM of the pyrite crystals had d-spacings of 0.27 nm. EDS analysis and a P map of the structures did not reveal any traces of organic material incorporated within the structures.

Blades structures and their alteration products (Fig. 19) were noted within 5 μm of the structures described above. The blades structures were interpreted to be volcanic glass as they were composed of a variety of elements and lacked crystal ordering (shown by HRTEM). The volcanic glass was found altering into a clay mineral (incipient stages in Rig.19a; later stage of alteration in Fig. 19b). Similar structures were found in JK03-036.

Mats on the southeast side of Vent 1 (JK04-025) contained no mineralization. Most of the cells are cocci less than 1 μm in diameter with some bacillus shaped prokaryotes (no evidence of a nucleus; Fig. 17p).

The largest silicified cells were found in an alcove on the southwest edge of the Vent 1 (Fig. 17l; JK03-037a). Most of the cells were greater than 2 μm in diameter and possibly surrounded by a thick capsule, which is typical of cyanobacteria (Westall et al. 2005). Strands extending from the surface of the cell (believed to be silicified EPS) were more thickly silicified than silicification occurring around the cell. Most of the larger cells had one layer of mineralization around the EPS, while the smaller cells typically did not.

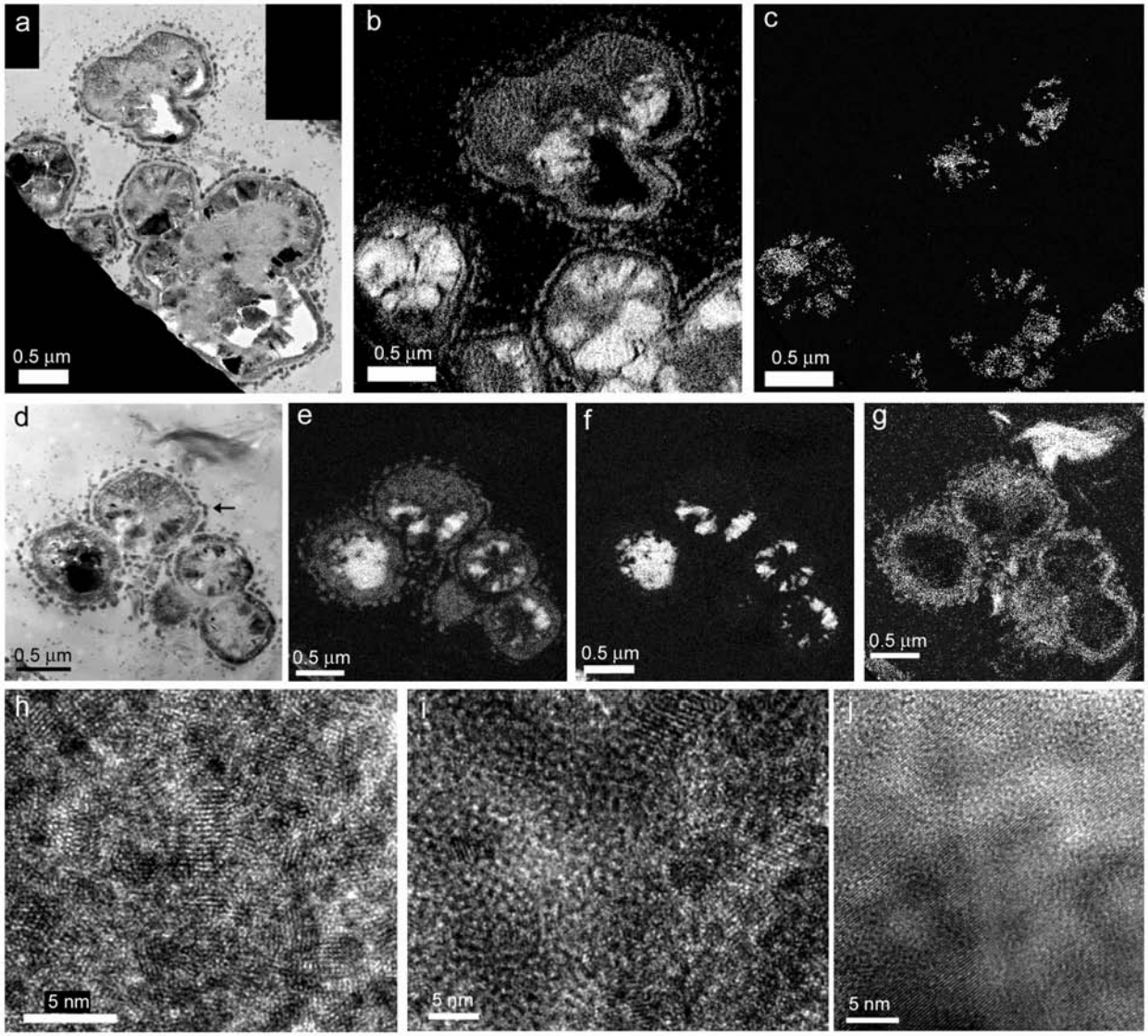

Figure 18. TEM EELS micrographs of structures found in JK04-024-b. Structure 1 (a-c) and structure 2 (d-g) are composed of iron oxides and iron sulfides. (b) Fe map and (c) S map of (a). (e) Fe map, (f) S map, and (g) oxygen map of (d). Bright white region in the upper right of (g) represents clay. Arrow in (d) is region of high resolution TEM (h-j). (h) Ferrihydrite spheres outside structures, (i) ferrihydrite inside structures, and (j) pyrite inside structures.

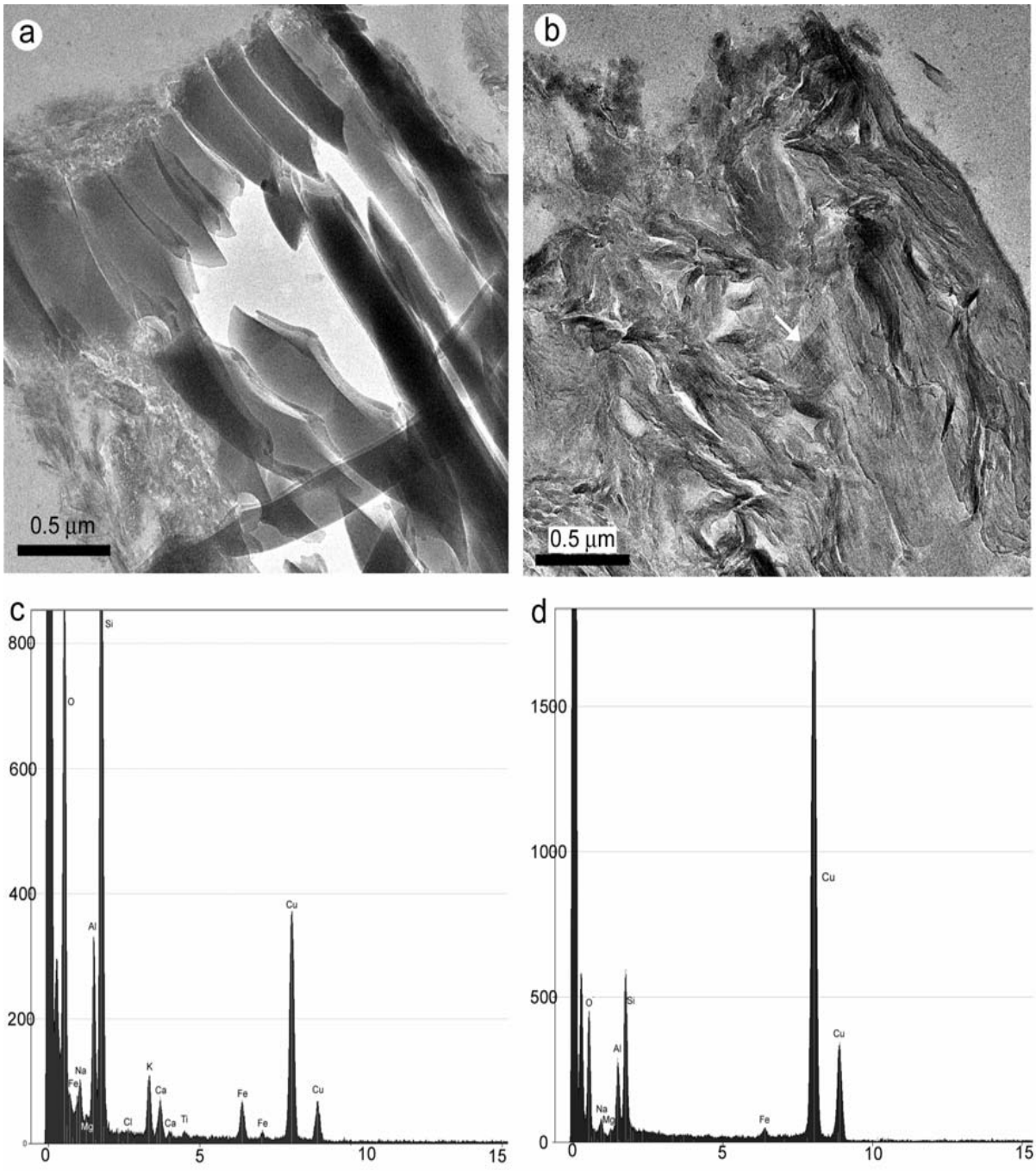

Figure 19. Volcanic glass (a) and clay minerals (b) found in JK04-024-b. The corresponding EDS spectra similar to volcanic glass (c) and clays (d) are in count/sec/energy (keV). The volcanic glass is shown altering into clay in the lower left of the micrograph (a), and remnants of the glass were noted in the clay (arrow) (b). Cu signal is due to copper grid used to stabilized the sections in the microscope. Conchoidal fracturing of the glass is an artifact from microtoming with a diamond knife.

CHAPTER 4

DISCUSSION

Typically, siliceous sinters form in near-neutral, alkali chloride type springs (Herdianita et al. 2000; Jones et al. 2000), although sinter formation within acidic springs (pH < 5) has been documented within the Waiotapu geothermal area of New Zealand (Jones et al. 2000). Jenn's Pools are between these two water types. Neutral-alkali springs can be characterized by the abundance of bacteria associated with the sinters that are formed almost entirely of opal-A with some calcite, whereas acid springs sinters are dominated by fungi and to a lesser extant diatoms and are composed of opal-A with substantial amounts of kaolinite, elemental sulfur, and/or jarosite (Jones et al. 2000). Jenn's Pools represents both spring types such that both springs contain abundant microbial mats composed mostly of prokaryotes (Fig. 17) but also contained substantial amounts of diatoms but with fungi found in Vent 1. Mineralogically, the underlying rocks from Vent 1 resemble those formed in acidic waters except for the presence of minor amounts of calcite, whereas Vent 2 underlying rocks were composed almost completely by opal-A.

Mineralogy

The sinters from both springs are likely relatively young. Little to no opal-A was transformed to more ordered silica polymorphs (opal-CT, opal-C, quartz) within the sinters. As mentioned above, representative diffractograms of opal-A are characterized by broad peak centered at 4.04 Å or 26° 2θ (see Fig. 6). This broad peak is indicative of a mineral phase with little long range order. Diffractograms of opal-CT, on the other hand, display a peak around 4.10

Å that is more narrow and intense than opal-A due to the onset of short-range ordering (Smith 1998). Some of these 4.10 Å peaks had a shoulder at 4.3 Å with the former representing ordering of a cristobalite like structure in the opal-CT structure and the latter representing a tridymite like structure. An additional, weaker peak for opal-CT occurs at 2.5 Å (Herdianita et al. 2000). All of the sinter collected from Jenn's Pools contained a weak peak at 4.04 Å and approximately two thirds contained a weaker peak at 2.5 Å, with only a slight thinning of the broad opal-A peak. This suggests that opal-A is in the incipient stage of development for short-range ordering to opal-CT. This interpretation was substantiated by the presence of highly amorphous opal-A structure with Al as a minor component of the sinters from JK03-007 (see Fig. 7). Although the underlying substrate sample for JK03-007 contains abundant kaolinite, neither XRD nor TGA analysis suggested the presence of this mineral phase in the sinter. Aluminum commonly substitutes for Si^{4+} in silica polymorphs, and given the noncrystalline nature of opal-A, Al substitution should occur readily when it is present in the environment. Al laminations within the sinters maybe related to the rate that silica is precipitated from solution. In highly saturated solutions, sinter laminations may be due to the amount of water within the opal-A structure (Jones and Renaut 2004). When opal-A deposits more rapidly, water content of the sinter increases, whereas opal-A that precipitates more slowly contains less water within it's structure (Jones and Renaut 2004). The same may also be true for the incorporation of trace elements into the opal-A structure.

Mineralogically, Vent 1 and Vent 2 were very similar except for the predominance of clays in the underlying rock of Vent 1 and opal-A in Vent 2. During the past two field seasons (2003 and 2004), spring fluid chemistry has remained relatively constant and similar. The cause for this difference in the alteration of andesine maybe attributed to Vent 1 being a sulfate type

spring, whereas Vent 2 is a mixed sulfate-chloride-bicarbonate spring. Acidic type springs have been shown to differ mineralogically from near neutral chloride type springs as discussed above. This alteration is believed to be due to sulfuric acid leaching and hydrothermal alteration of the volcanic rocks (Jones et al. 2000). Vent 1 also resembles an acidic type system such it contained minerals such as cinnabar, elemental gold, and cassiterite which are commonly found in hydrothermal acid-sulfate systems (Guilbert and Park 1986).

The alteration of andesine to kaolinite (Eq. 2, 4, 6) and halloysite (Eq. 3, 5, 7) only occurred around the rims of Jenn's Pools, not within the spring itself where silica polymorphs dominated (Table 2). This difference maybe due the presence of abundant microbial mats. Given the pH at Jenn's Pools is 5.3 to 5.9, abiotic weathering of silicates is low (Chou and Wollast 1985; Welch and Ullman 1993, 1996). Aluminosilicate dissolution can be increased by two orders of magnitude by bacterial production of organic and inorganic acids and EPS used in attachment (Barker et al. 1998). The rim of Vent 1 is lined with green microbial mats, and the spring floor up to and lining the rim (Fig. 5b) is covered with primary colonizers including hydrogen-oxidizers (private communication, Reysenbach). Hydrogen-oxidizing thermophilic chemolithoautotroph when under anaerobic conditions can produce hydrogen sulfide:

[1] $$H_2 + S^0 \rightarrow H_2S$$

The production of inorganic acids such as carbonic acid (Eq. 2-3) through microbial respiration of organic matter (Schwartzman and Volk 1989, 1991), and the production of reduced sulfur compounds (Eq. 4-5) at the rock/microbial mat interface by lithotrophic microbes also enhances weathering rates (Barker et al. 1997). Organic acids produced by bacteria and fungi, although weak acids, increase dissolution by protons and organic ligands weakening silicate bonds

(Barker et al. 1997; Eq. 6-7). Organic acids are depicted as oxalic acid (CHO2) in equation 6 and 7 as this acid is known to weather silicate rocks (Barker et al. 2003).

[2] $2NaAlSi_3O_8 + 2H_2CO_3 + 9H_2O \rightarrow Al_2Si_2O_5(OH)_{4(s)} + 2Na^+ + 2HCO_3^- + 4H_4SiO_{4(aq)}$

[3] $2NaAlSi_3O_8 + 2H_2CO_3 + 10H_2O \rightarrow Al_2Si_2O_5(OH)_4 \cdot H_2O_{(s)} + 2Na^+ + 2HCO_3^- + 4H_4SiO_{4(aq)}$

[4] $2NaAlSi_3O_8 + H_2S + 9H_2O + 2O_2 \rightarrow Al_2Si_2O_5(OH)_{4(s)} + 2Na^+ + SO_4^{2-} + 4H_4SiO_{4(aq)}$

[5] $2NaAlSi_3O_8 + H_2S + 10H_2O + 2O_2 \rightarrow Al_2Si_2O_5(OH)_4 \cdot H_2O_{(s)} + 2Na^+ + SO_4^{2-} + 4H_4SiO_{4(aq)}$

[6] $2NaAlSi_3O_8 + 2CH_2O + 10H_2O + \frac{1}{2}O_2 \rightarrow Al_2Si_2O_5(OH)_{4(s)} + 2Na^+ + 2HCO_3^- + 4H_4SiO_{4(aq)}$

[7] $2NaAlSi_3O_8 + 2CHO_2 + 11H_2O + \frac{1}{2}O_2 \rightarrow Al_2Si_2O_5(OH)_4 \cdot H_2O_{(s)} + 2Na^+ + 2HCO_3^- + 4H_4SiO_{4(aq)}$

Pyrite is also commonly associated with the clay phases. The orthopyroxene components (Eq. 8) within andesite and/or volcanic glass (Eq. 9) both could have formed pyrite by the following reactions:

[8] $Fe(SiO_3)_2 + 2H_2S + 2H_2O \rightarrow FeS_2 + 2H_4SiO_{4(aq)}$

[9] $2(Na,Ca,K)(Al,Mg,Fe,Ti)SiO_2 + 2H_2S + 5H_2O \rightarrow FeS_2 + Al_2Si_2O_5(OH)_{4(s)} + 2Na^+ + 2Ca^{2+} + 2K^+ + 2Mg^{2+} + 2Ti^+ + Fe^{2+} + 10H^+$

Equation 9 also applies to the volcanic glass altering to clay embedded within the mat samples. Hydrogen sulfide maybe originating from the same source as that reducing ferrihydrite in iron-bearing structures. These processes are described below.

Biomineralization

A variety of the mineral assemblages identified are known to be produced through BIM and/or BCM. Morphological evidence through SEM and TEM suggests BIM is the predominant form of biological mineralization occurring in Jenn's Pools. Many of the cells undergoing silicification by colloidal opal-A have died and cellular material has since degraded leaving an extracellular silicified molds as the only evidence of microbial activity (Fig. 14 and 17). Silicification has been shown to not necessarily be immediately detrimental to a cell's viability (Phoenix et al. 2000). Many live cells (defined here as the presence of internal cellular components and intact cell wall) were undergoing silicification on the outer surface the cell along the EPS. Phoenix et al. (2000) found that the cyanobacterium *Calothrix* sp. was able to thrive in silica saturated environments where mineralization takes place on the outer surface of the sheath (made up of EPS surrounding the cell) enabling the cell to conduct vital metabolic processes across the cell wall. The sheath acted as an alternative nucleation site preventing cell wall and cytoplasmic mineralization. Once the cell wall was mineralized, the cells were no longer healthy (Phoenix et al. 2000). In the mat samples analyzed from Jenn's Pools, cell wall mineralization only occurred when the EPS surrounding the cell contained a thick siliceous crust. It is suggested here that the EPS was mineralized first given it is directly exposed to the environment, and the cell wall was mineralized second due to a breakdown in the EPS structure (Fig. 17b). Silicification of EPS isolates the cell from the surrounding environment blocking net water flow and nutrient supply from the environment to the cell, and causing a build up of metabolic byproducts excreted by the cell. These direct effects of silicification would cause the cell to become unhealthy, and result in a decrease in cellular functions. Given EPS have a hydrous structure (Sutherland 2001), a loss in net water supply to the cell would cause EPS to

dehydrate, possibly causing it to lose structure. This breakdown in the EPS structure may allow smaller opal-A sphere to pass through the EPS layer and nucleate to the cell wall. Phoenix et al. (2000) come to similar conclusions when studying silicification of cyanobacterium *Calothrix* sp., such that once the cell becomes unhealthy and lysis occurs, colloidal silica is able to penetrate the sheath and mineralize the cell wall.

Cells that underwent the greatest silicification were in alcoves near the vents. Vent 2 samples collected from the northwest side of the vent were affected by the surging of the spring where the heaviest mineralized mat was collected near surge maximum (JK04-019). Given that spring fluids are undersaturated with silica, for opal-A to precipitate and form thick crusts, concentration of the silica through evaporation must be occurring. Mats facing the spring were the most silicified, whereas on the opposite edge of the same sample the mat were only lightly mineralized. The other region that underwent intense silicification was from the west side of Vent 1. The cells, although not thickly mineralized, were silicified around the cell and EPS strands extending away from the cell (Fig. 17q). A study conducted by Chan et al. (2004) deduced that polysaccharides excreted from the cell localize precipitation reactions in which the silicified polymer was later detached from the cell. One implication of this study was that the mineralized strands were discarded to prevent cellular entombment. This argument may also apply to the silicified and the unattached EPS strands noted above. The EPS extending outward from the cell contained a majority of the silicification away from the cell surface, which appeared detached from the cell. It is also possible that detached appearance from the Jenn's Pools samples was due to a three dimensional structure being viewed in 2 dimensions through the TEM, or a result of the fixation process causing detachment of the silicified strands.

The other implication from the Chan et al. (2004) study was the oxidation of iron

immediately outside the cell would "increase the pH gradient across the cell membrane by 2 to 4 H^+ per ferrous iron oxidized," enhancing metabolic processes. Ferrihydrite spheres attached to cell wall like morphologies from the southwest side of Vent 1 (Fig. 17o and 18) may have created similar microenvironments at Vent 1. These structures were collected within a microbial mat attached to the side of a spicule. A space exists between the ferrihydrite spheres on the outside of the structure and the spherical structures themselves which at one time could have been an EPS layer surrounding that cell or the cell wall that has since degraded. Sections of mat analyzed above this iron-bearing section may have contained phototrophic species (intracellular membranes located with prokaryotic cells are believed to be related to phototrophic processes) (Fig. 17m, n). Given that under constant conditions metabolic pathways can alter dramatically within millimeters of a mat, iron oxidizers could have created the spherical iron-bearing structures. When the cells were alive, ferrihydrite bound extracellularly as a byproduct of cell respiration. The gap between the ferrihydrite spheres outside the cell and ferrihydrite within the cells suggests that ferrihydrite began to replace the organic material within the cell presumably as the cell was dying or quickly after cell death. Pyrite within the cells is believed to have formed as hydrogen sulfide came through the system by either sulfur reducing bacteria or from gasses emitted from the springs reducing the ferrihydrite.

Intracellular iron-bearing mineral phases have been shown to be produced by a metal-reducing, anaerobic bacterium *Shewanella* sp. in an experiment conducted by Glasauer et al. (2002), in which the bacterium uses mineral-bound ferrihydrite as a terminal electron acceptor (Glasauer et al. 2002). The fine grained aggregates of ferrihydrite adsorbed to the surface of *Shewanella putrefaciens* was the source of cellular iron. Less than a week after ferrihydrite was introduced into the growth medium of *S. putrefaciens*, Fe^{2+} was detected and intracellular iron

oxide granules began to form within the cytoplasm. The intracellular granules first formed near the cytoplasm and grew inward towards the center of the cell as if the granules were being "pushed into the cytoplasm as subsequent granules developed." As iron oxide granules accumulated within the cell, crystalline and poorly crystalline ferrihydrite (d-spacing of 0.15 nm and 0.25 nm) were observed extracellularily. If these cells were to die, losing all cellular components, the cells may resemble the iron-bearing structures described above from Vent 1 mat (Fig. 17o and 18). Ferrihydrite was found intracellularly, and in some instances lining what may have been the plasma membrane, with pyrite forming around the center of the cell structures. Crystalline and poorly crystalline ferrihydrite granules were also attached to the outside of the cell structure where they would be available as a terminal electron acceptor during respiration. Pyrite is presumed to have formed after cell death as ferrihydrite reacts with hydrogen sulfide from either sulfate reducing bacteria (SRB) or gas emitted from spring fluids.

The function of the intracellular iron oxide granules is under speculation although, current thought is that ferrihydrite maybe essential for growth or a growth byproduct (Glasauer et al. 2002).

The only other form of possible BIM was from the heavily mineralized mats from Vent 2 (Fig. 17e). Although no elemental analysis was conducted, the structures resemble volcanic glass and clays found in another section (Fig. 19). Since no cellular material was found, if these structures were the product by BIM, the cells would have mineralized extracellularly. Close up images of the alteration phase forming around the structures resembles stacked kaolinite plates (Fig. 10a), although an order of magnitude smaller. Clays, such as smectites, with high buffering capacity and high cation exchange capacity (CEC) have been shown to stimulate microbial respiration for a variety of soil bacteria through maintaining near neutral pH for cell growth

(Stotzky and Rem 1966; Stotzky 1966). Kaolinite on the other hand, has little to no effect on respiration due to it's low buffering capacity and low CEC (Stotzky and Rem 1966; Stotzky 1966). Some stimulation is noted by the shortening of lag time during microbial growth, but not as much as montmorillonite (Stotzky and Rem 1966).

Manganese oxide was noted associated with a microbial cell (JK04-037) which could have formed by the following bacterial oxidation reactions (Ehrlich 1990):

[11] $2Mn^{2+} + 1/2O_2 + 2H^+ \rightarrow 2Mn^{3+} + H_2O$

[12] $2Mn^{3+} + 1/2O_2 + 3H_2O \rightarrow 2MnO_2 + 6H^+$

The difference in elemental analysis through EDS of the crystal and rods residing on it was the presence of manganese associated with the microbial forms. Presence of extracellular mineralization was not visually noted although some of the cells surfaces appeared rough (upper left of Fig. 20).

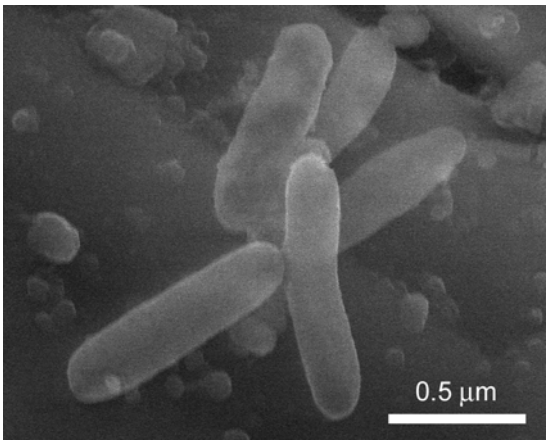

Figure 20. Manganese oxide found in presence of these cells on a pyroxene crystal from Vent 1

Possible advantages of extracellular mineralization include protection from physical damage (high intensity sunlight, Wyman and Fay 1986), and predation from toxin producing microorganisms (Habte and Barrion 1984) and grazing protozoans (Heijnen et al. 1992). Extracellular molds could also protect from the above as microorganism take refuge within the molds (Fig. 17g). If the molds were near the surface of a microbial mat exposed to the atmosphere they would offer some protection and stability from adverse climatic conditions and sunlight.

Microbe-Mineral Interactions

The most prominent physical microbial-mineral interaction within Jenn's Pools is the association of silica with microorganisms. This relationship has no known metabolically benefit for the microbes, only a protective benefit. The second most common microbe-mineral interaction was between iron-bearing phases and microorganisms and microbial byproducts (EPS). Microorganisms were continuous found in direct contact with iron-bearing phases (Fig. 12b) or attached through the extension of EPS (Fig. 12), but were rarely or never found associated with barite or titanium-bearing mineral phases, respectively. Although the microbial species within the system are for the most part unknown, certain assumptions can be made based on these relationships. Of the mineral phases identified within the sinters, iron sulfides and iron oxides can be used directly in electron transfer reactions to extract energy from the environment for metabolic processes such as iron oxidation (Eq. 13-14; Singer and Stumm 1970) and iron reduction (Eq. 15).

[13] $FeS_2 + 7/2O_2 + H_2O \rightarrow Fe^{2+} + 2H^+ + 2SO_4^{2-}$

[14] $Fe^{2+} + 1/2O_2 + 2H^+ \rightarrow Fe^{3+} + H_2O$

[15] $2Fe(OH)_3 + 2H_2S + 2H^+ \rightarrow FeS_2 + 6H_2O + Fe^{2+}$

Barite, on the other hand, would form as a result sulfate forming through either sulfide oxidation or from spring fluid reactions with the surrounding parent rock. Given both barite and gypsum have been found in the sinters and associated with the microbial mats, sulfate must be abundant. Under sulfate-depleted conditions in marine sediments, sulfate reduction causes the dissolution of barite (Kasten and Jorgensen 2000). Barium ions in solution may migrate upward to sulfate-rich zones and reform barite or react with bicarbonate ions in solution to form witherite. Although, barite is assumed to have formed as a reaction with dissolved sulfate within the

system, recently a bacterium found in soil and marine environments, *Myxococcus xanthus*, has been shown to possibly mediate the production of barite crystals under laboratory conditions (González-Muñoz et al. 2003). The barite crystals precipitated were similar in size or larger than the barite crystals found within Jenn's Pools. Precipitates found within the culture were heavily associated with phosphous which was interpreted to be due PO_4^{3-} ligands within the cell wall favoring Ba^{2+} sorption (González-Muñoz et al. 2003). As SO_4^{2-} content within the culture increased (sulfate suggested to result from the degradation and oxidation of amino acids), the ions were captured by Ba^{2+}, causing a barite growth nucleus. In experiments conducted using dead *M. xanthus*, no barite was produced.

Ti-bearing mineral phases were not found to be associated with microbial cells possibly due to one of three reasons: (1) there is no metabolic benefit for the microorganisms, (2) the Ti-bearing phases are toxic to the cells, and/or (3) the Ti-bearing mineral phases were relatively newly formed as amorphous ilmenite has been shown to be produced through BIM and/or BCM (Weiner and Dove 2003).

Pinnularia sp. diatoms (Fig. 12k) were abundant in both microbial mats from both springs. This diatom species is often abundant in nutrient poor waters (http://www.biol.paisley.ac.uk/bioref/Chromista/Pinnularia.html), and can live up to 35° C to 50° C (Wehr and Sheath 2003). The presence of *Pinnularia* suggests diatoms are competing with other heterotrophs for nutrients, or organic nutrients within a nutrient-poor ecosystem. With low levels of organic matter available, obtaining nutrients by other metabolic means such as chemolithoautotrophy maybe a common method of acquiring energy.

Preservation of microbial activity

Six out of the eight criteria for evidence of past life listed on page 8 are met by this study. The two criteria that were not met were finding evidence of biominerals showing chemical or mineral disequilibrium, and stable isotope analysis which was not conducted. If the sinters and underlying rocks examined in Jenn's Pools were reexamined thousands of years from now with environmental conditions remaining constant (this is a large assumption), some of the evidence noted today may be preserved. Toporski et al., (2002) suggest that in a closed system were temperature and pressure remained constant, silicified microbes are unlikely to undergo *in situ* dissolution/reprecipitation reactions enabling the silicified microfossils to become preserved for longer periods of time. Although this statement is generally agreed upon, the amount of silicified microbes with the microbial mats is far more abundant than the extracellular silicified molds found within the sinters. Time is also an important factor in silica polymorph dissolution/reprecipitation reactions (Fournier 1985). The dissolution/reprecipitation reaction of opal-A to quartz can occur over this time frame, which may destroy most extracellular silicified molds (Fig. 17) as opal-A dissolves back into solution. The mineralogy and textures of sinters modern to Miocene in age were found to changed through time as opal-CT and quartz formed from opal-A and fossilized microbial filaments were modified or destroyed (Herdianita et al. 2000). Depending on the rate of dissolution/reprecipitation reaction, some of the molds maybe preserved if the dissolution/reprecipitation reaction occurs on the submicron scale although fine scale detail will be lost. Silicified tubes maybe preserved if an internal mold was made but there is no evidence of this presently occurring.

The iron-bearing structures found within Vent 1 mat (Fig. 17o and 18) will probably be preserved within the rock record. The mineralogy of the structures may change as the surrounding conditions alter through time but the morphology of the structures will most likely

remain.

The sulfur-bearing curved segments (Fig. 16) are also likely to be preserved given that they are already preserved within the underlying rock. The only question that remains is if the formation of the these structures were bacterially mediated. Isotope analysis is required to provide further insights into the origin of these features.

Finally, the filamentous structures observed in the sinter and the underlying rock (Fig. 15) are unlikely to be preserved within the next few thousand years as most of the organic components will probably degrade and be recycled back into the environment. Although a morphological signature will likely be lost, recent studies suggest a chemical signature may be preserved within sinters as modern siliceous sinters from New Zealand have been shown to preserve lipid material (Pancost et al. 2005).

CHAPTER 5

CONCLUSIONS

Microbial activity had a major impact on the mineral assemblages noted within Jenn's Pools and visa versa. Clay alteration of the underlying rock was only noted in regions that contained abundant microbial mats along the rim of Vent 1 where weathering of aluminosilicates can be increased by two orders of magnitude through microbial activity.

Extracellular silicification was the most common form of biomineralization although it is unlikely to be preserved within the rock record as opal-A dissolves back into solution and reprecipitates as more ordered silica polymorphs altering and/or destroying most of the silicified molds. In addition to silica being the primary form of biomineralization, it is also the most common inorganic phase to interact with microbial cells and/or the byproducts. This relationship is believed to be so prominent because microbial cells and their byproducts often act as nucleation sites for sinter formation, and opal-A the dominant mineral phase composing the sinters which is used as substratum for microbial mat formation. The second most common mineral-microbe interaction is between microbial cells and iron-bearing mineral phases. Many of the iron-bearing mineral phases were directly associated with microbes in which iron could be utilized for metabolic purposes or the mineral phases formed as a result of microbial activity.

The ferrihydrite and pyrite structures found within a Vent 1 mat are believed to have been formed by the respiration of iron oxidizers and later iron replacement of those cells. Questions still exist on how the cells underwent iron replacement so soon after cell death and how the oxidation/reduction gradient of iron mineral phases formed. Of all of the morphological

remnants of microbial activity identified within Jenn's Pools, these iron-bearing structures are the only structures that will likely be preserved within the rock record and potentially identified as past life.

The presence of diatoms that commonly form in nutrient poor systems indicates that chemolithoautotrophy may be a common method of acquiring energy for prokaryotic species within the mats.

Future work on these samples to better characterize their preservation potential would be to conduct stable isotope and lipid analysis to reveal the isotopic and biomarkers signature, respectively. Also, laboratory analysis on the effects opal-A dissolution and opal-CT precipitation on extracellular silicified molds would offer further insight into the destruction or possible preservation of these molds.

REFERENCES

Altermann, W. 2001. The oldest fossils of Africa- a brief reappraisal of reports from Archean. African Earth Sciences, **33:** 427-436.

Aguiar, P., Beveridge, T.J., and Reysenbach, A.-L. 2004. *Sulfurihydrogenibium azorense*, sp. nov., a thermophilic hydrogen-oxidizing microaerophile from terrestrial hot springs in the Azores. International Journal of Systematic and Evolutionary Microbiology, **54:** 33-39.

Barker, W.W., Welch, S.A., and Banfield, J.F. 1997. Biogeochemical weathering of silicates minerals. *In* Geomicrobiology: Interactions between microbes and mineral. Ed. J.F. Banfield and K.H. Nealson. **35:** 391-428.

Bazylinski, D.A., and Frankel, R.B. 2003. Biologically Controlled Mineralization by Prokaryotes. *In* Biomineralization. *Edited by* P.M. dove, J.J. De Yoreo, and S. Weiner. Reviews in Mineralogy and Geochemistry, **54:** 217-247.

Bennett, P.C., and Engel, A.S. 2004. Imaging and Counting Microorganisms on Rocks, Clay Mineralogical Society Microbe-Mineral Interactions Workshop.

Brasier, M.D., Green, O.R., Jephcoat, A.P., Kleepe, A.K., Van Kranendonk, M.J., Lindsay, J.F., Steele, A., Grassineau, N.V. 2002. Questioning the evidence of Earth's oldest fossils. Nature, **416:** 76-81.

Braunstein, D., and Lowe, D.R. 2001. Relationship between spring and geyser activity and the deposition and morphology of high temperature (> 73 °C) siliceous sinter, Yellowstone National Park, Wyoming, U.S.A. Journal of Sedimentary Research, **71:** 747-763.

Brown, L.D., Ray, A.S., Thomas, P.S., and Guerbois, J.P. 2002. Thermal characteristics of Australian sedimentary opals. Journal of Thermal Analysis and Calorimetry, **68:** 31-36.

Cady S.L., and Farmer, J.D. 1996. Fossilization processes in siliceous thermal springs: trends in preservation along thermal gradients. In: Evolution of hydrothermal ecosystems of Earth (and Mars?) Wiley, Chichester (Ciba Foundation Symposium 202), pp. 150-173.

Chan, C.S., De Stasio, G., Welch, A.A., Girasol, M., Frazer, B.H., Nesterova, M.V., Fakra, S., and Banfield, J.F. 2004. Microbial Polysaccharides Template Assembly of Nanocrystal Fibers. Science, **303:** 1656-1658.

Chou, L., and Wollast, R. 1985. Steady-stae kinetics and dissolution of albite. American Journal

of Science, **285:** 963-993.

Crowe, D.E., and Karpov, G.A. 2004. Geologic Setting of the Uzon Caldera, Kamchatka, Far East Russia. Geological. Society of America Abstracts with Programs, **36:** 432.

Edwards, M.R., and Gantt, E., 1971. Phycobilisomes of the thermophilic blue-green alga *Synechococcus lividus*. Journal of Cell Biology, **50:** 896-900.

Enrlich, H.L. 1990. Geomicrobiology. Marrcel Dekker. New York, N.Y., 2nd Ed., p.646.

Ferris, F.G., Fyfe, W.S., and Beveridge, T.J. 1988. Metallic ion binding by *Bacillus subtilis*: Implications for the fossilization of microorganisms. Geology, **16:** 149-152.

Fortin, D., and Beveridge, T.J. 2000. Mechanistic routes towards biomineral surface development. *In* Biomineralization: From Biology to Biotechnology and Medical Application. Edited by Edmund Baeuerlein. Wiley-VCH, Verlag, Germany, pp. 7-24.

Fournier, R.O. 1985. The behavior of silica in hydrothermal solutions. Review in Economic Geology, **2:** p. 45-61.

Founier, R.O., and Rowe, J.J. 1966. Estimation of underground temperatures from the silica content of water from hot springs and steam wells. American Journal of Science, **264:** 685-697.

Frankel, R.B., and Bazylinski, D.A. 2003. Biologically Induced Mineralization by Bacteria. *In* Biomineralization. *Edited by* P.M. dove, J.J. De Yoreo, and S. Weiner. Reviews in Mineralogy and Geochemistry, **54:** 95-114.

Gibson, E.K., McKay, D.S., Thomas-Keprta, K.L., Wentworth, S.J., Westall, F., Steele, A., Romanek, C.S., Bell, M.S., and Toporski, J. 2001. Life on Mars: evaluation of the evidence within Martian meteorite ALH84001, Nakhla, and Shergotty. Precambrian Research, **106:** 15-34.

Glasauer, S., Langley, S., and Beveridge, T.J. 2002. Intracellular Iron Minerals in a Dissimilatory Iron-Reducing Bacterium. Science, **295:** 117-119.

González-Muñoz, M.T., Fernández-Luque,B., Martínez-Ruiz, F., Chekroun, K., Arias, J.M., Rodríguez-Gallego, M., Martínez-Canamero, M., de Linares, C., and Paytan, A. 2003. Precipitation of Barite by *Myxococcus xanthus*: Possible Implications for the Biogeochemical Cycle of Barium. Applied and Environmental Microbiology, **69:** 5722-5725.

Guilbert, J. M., and Park, C. F. 1986. The geology of ore deposits. W. H. Freeman, New York.

Habte, M., and Barrion, M. 1984. Interactions of *Rhizobium* sp. with toxin producing fungus in culture medium and in a tropical soil. Applied Environmental Microbiology. **47:** 1080-

1083.

Heijnen, C.E., Hok-A-Hin, C.H., and van Veen, J.A. 1992. Improvements to the use of bentonite clay as a protective agent, increasing survival levels of bacteria introduced into soil. Soil Biological Biochemistry, **24:** 533-538.

Herdianita, N.R., Browne, P.L., Rodgers, K.A, and KA. Campbell, 2000. Mineralogical and textural changes accompanying ageing of silica sinter. Mineralium Deposita, **35:** 48-62.

Hollingsworth, E.R., Crowe, D.E.**,** and Romanek, C.S. 2004. Hydrothermal alteration facies in the Uzon Caldera, Kamchatka, Far East Russia. Geological Society of America Abstracts with Programs, **36:** 432.

Janney, D.E., Cowlee, J.M., and Buseck, P.R. 2000. Structure of synthetic 2-line ferrihydrite by electron nanodiffraction. American Mineraologist, **85:** 1180-1187.

Jones, B., and Renaut, R.W. 1996. Influence of thermophilic bacteria on calcite and silica precipitation in hot springs with water temperatures above 90 °C: evidence from Kenya and New Zealand. Canadian Journal of Earth Science, **33:** 72-83.

Jones, B., and Renaut, R.W**.** 2004. Water content of opal-A: implications for the origin of laminae in geyserite and sinter. Journal of Sedimentary Research, **74:** 117-128.

Jones, B., Renaut, R.W. and Rosen, M.R. 1997. Biogenicity of silica precipitation around geysers and hot spring vents, North Island, New Zealand. Journal of Sedimentary Research, **67:** 88-104.

Jones, B., Renaut, R.W., and Rosen, M.R. 2000, Stromatolite Forming in Acid Hot-Spring Waters, North Island, New Zealand. Palaios, **15:** 450-475.

Jones, B., Renaut, R., and Rosen, M. 2001. Taphonomy of Silicified Filamentous Microbes in Modern Geothermal Sinter- Implications for Identification. Palaios, **16:** 580-592.

Jones, C.A., Crowe, D.E., and Romanek, C.S. 2004. Geothermal fluid source determination in the Uzon Caldera, Kamchatka, Russia. Geological Society of America Abstract with Programs, **36:** 432.

Karpov, G.A. 1995. WRI-8 Post Session Field Trip to Kamchatka Part II: Uzon-Geyser Depression. *In* Proceedings of the 8th international symposium on water-rock interaction (WRI-8), Vladivostok, Russia, pp. 31-33.

Karpov, G.A. 1998. Uzon: A Protected Land.

Karpov, G.S., and Naboko, S.I. 1990. Metal contents of recent thermal waters, mineral precipitates and hydrothermal alteration in active geothermal fields, Kamchatka. Journal of Geochemical Exploration, **36:** 57-71.

Kasten, S., and Jorgensen, B.B. 2000. Sulfate Reduction in Marine Sediments. *In* Marine Geochemistry. *Edited by* H.D. Schulz, and M. Zabel. Spring-Verlag, New York, pp.263-281.

Konhauser, K.O., Jones, B., Reysenbach, A., and Renaut, R.W. 2003. Hot spring sinters: keys to understanding Earth's earliest life forms. Canadian Journal of Earth Science, **40:** 1713-1724.

Konhauser, K.O., Phoenix, V.R., Bottrell, S.H., Adams, D.G., and Head, I.M. 2001. Microbial-silica interactions in Icelandic hot spring sinter: possible analogues for some Precambrian siliceous stromatolites. Sedimentology, **48:** 415-433.

Lowenstam, H.A. 1981. Minerals formed by organisms. Science **211:** 1126-1130.

Mann, S. 1983. Mineralization in biological systems. Structural Bonding, **54:** 125-174.

McKay, D.S., Gibson, E.K., Thomas-Keprta, K.L., Vali, H., Romanek, C.S., Clemett, S.J., Chillier, X., Maechling, C.R., and Zare, R.N. 1996. Search for Past Life on Mars: Possible Relic Biogenic Activity in Martian Meteorite ALH84001. Science, **273:** 924-930.

Mera, M.U., and Beveridge, T.J. 1993. Mechanism of Silicate Binding to the Bacterial Cell Wall in *Bacillus subtilis*. Journal of Bacteriology, **175:** 1936-1945.

Mountain, B.W., Benning, L.G., and Boerema, J.A., 2003. Experimental studies on New Zealand hot spring sinters: rates of growth and textural development. Canadian Journal of Earth Sciences, **40:** 1643-1667.

Pancost, R.D., Pressley, S., coleman, J.M., Benning, L.G., and Mountain, B.W. 2005. Lipid biomolecules in silica sinters: indicators of microbial biodiversity. Environmental Microbiology, **7(1):** 66-77.

Phoenix, V.R., Adams, D.G., and Konhauser, K.O. Cyanobacterial viability during hydrothermal biomineralization. Chemical Geology, **169:** 329-338.

Prescott, L.M., Harley, J.P., and Klein, D.A. 2002. Microbiology, 5th edition. McGraw-Hill Companies, Inc., New York, N.Y.

Renaut, R.W., Jones, B., and Tiercelin, J.J. 1998. Rapid *in situ* silicification of microbes at Loburu hot springs, Lake Bogoria, Kenya Rift Valley. Sedimentology, **45:** 1083-1103.

Rice, S.B., Freud, H., Huang, W.L., Clouse, J.A., and Isaacs, C.M., 1995. Applications of Fourier Transform Infrared Spectroscopy to Silica Diagenesis: The opal-A to opal-CT Transformation, Journal of Sedimentary Research, **A65**, 639-647.

Rimstidt, J.D., and Cole, D.R. 1983. Geothermal mineralization I: The mechanism of formation of the Beowawe, Nevada, siliceous sinter deposit. American Journal of Science, **283:** 861-875.

Romanek, C.S., Crowe, D.E., Kyle, J., and Schroeder, P.A. 2004. Chemical and stable isotopic composition of microbial mats from hot springs of Uzon Caldera, Kamchatka. Geological Society of America Abstracts with Programs, **36:** 474.

Romanek, C.S., Grady, M.M., Wright, I.P., Mittlefehldt, D.W., Socki, R.A., Pillinger, C.T., and Gibson, E.K. 1994. Record of fluid-rock interactions of Mars from the meteorite ALH84001. Nature, **372:** 655-657.

Rosing, M.T., 1999. 13C-Depleted Carbon Microparticles in > 3700-Ma Sea-Floor Sedimentary Rocks from West Greenland. Science, **283:** 674-676.

Schopf, J.W., and Packer, B.M., 1987. Early Archean (3.3-Billion to 3.5-Billion-Year-Old) Microfossils from Warrawoona Group, Australia. Science, **237:** 70-73.

Schopf, J.W. 1993. Microfossils of the Early Archean Apex Chert: New Evidence of the Antiquity of Life. Science, **260:** 640-646.

Schultze-Lam, S., Ferris, F.G., Konhauser, K.O., and Wiese, R.G. 1995. In situ silicification of an Icelandic hot spring microbial mat: implications for microfossil formation. Canadian Journal of Earth Sciences, **32:** 2021-2026.

Schwartzman, D.W., and Volk, T. 1989. Biotic enhancement of weathering and the habitability of Earth. Nature, **340:** 457-459.

Schwartzman, D.W., and Volk, T. 1991. Biotic enhancement of weathering and surface temperatures on Earth since the origin of life. Paleogeography, Paleoclimate, Paleoecology, **90:** 357-371.

Shen, Y., Buick, R., and Canfield, D. 2001. Isotopic evidence for microbial sulfate reduction in the early Archaean era. Nature, **410:** 77-81.

Silverside, A.J. 2003. Citing online source: Pinnularia [online]. Available from http://www-biol.paisley.ac.uk/bioref/Chromista/Pinnularia.html.

Singer, P.C., and Stumm, W. 1970. Acidic mine drainage. Science, **167:** 1121-1123.

Smith, D.K. 1998. Opal, Cristobalite, and tridymite: noncrystallinity versus crystallinity, nomenclature of the silica minerals and bibliography. Powder Diffraction, **13:** 2-29.

Stotzky, G. 1966. Influence of clay minerals on microorganisms III. Effect of particle size, cation exchange capacity, and surface area on bacteria. Canadian Journal of Microbiology. **12:** 1235-1246.

Stotzky, G., and Rem, L.T. 1966. Influence of clay minerals on microorganisms I. Montmorillonite and kaolinite on bacteria. Canadian Journal of Microbiology, **12:** 547-563.

Sutherland, I.W. 2001. Biofilm exopolysaccharides: a strong and sticky framework.

Microbiology, **124:** 3-9.

Toporski, J., Steele, A., Westall, F., Thomas-Keprta, K., and McKay, D. 2002. The Simulated Silicification of Bacteria- New Clues to the Modes and Timing of Bacterial Preservation and Implications for the Search for Extraterrestrial Microfossils. Astrobiology, **2(1):** 1-26.

van Zuilen, M.A., Lepland, A., and Arrhenius, G., 2002. Reassessing the evidence for the earliest traces of life. Nature, **418:** 627-629.

Walsh, M.M. 1992. Microfossils and possible microfossils from the Early Archean Onverwacht Group, Barberton Mountain Land, South Africa. Precambrian Research, **54:** 271-292.

Walsh, M.M, and Lowe, D.R., 1985. Filamentous microfossils from the 3500 Myr0old Onverwacht Group, Barberton Mountain Land, South Africa. Nature, **314:** 530-532.

Weiner, S., and Dove, P. 2003. An Overview of Biomineralization Processes and the Problem of the Vital Effect. *In* Biomineralization. *Edited by* P.M. dove, J.J. De Yoreo, and S. Weiner. Reviews in Mineralogy and Geochemistry, **54:** 1-24.

Welch, S.A., and Ullman, W.J. 1993. The effect of organic acids on plagioclase dissolution rates and stoichiometry. Geochimica et Cosmochimica Acta, **57:** 2725-2736.

Welch, S.A., and Ullman, W.J. 1996. Feldspar dissolution in acidic and organic solutions. Geochimica et Cosmochimica Acta,**60:** 2939-2949.

Westall, F., Boni, L., and Guerzoni, E. 1995. The experimental silicification of microorganisms. Palaeontology, **38:** 495-528.

Westall, F., de Wit, J., Dann, J., van der Gaast, S., de Ronde, C., and Gerneke, D., 2001. Early Archean fossil bacteria and biofilms in hydrothermally-influended sediments from the Barberton greenstone belt, South Africa. Precambrian Research, **106:** 93-116.

Westall. F. 2005. Early Life on Earth and Analogies to Mars. *In* Water on Mars and Life, Edited by T. Tokano. SpringerVerlag Berlin Heidelberg. Pp. 45-64.

Wyman, M., and Fay, P. 1986. Underwater light climate and the growth of pigmentation of planktonic blue-green algae (Cyanobacteria): I. The influence of light quantity. Proceeding of the Royal Society of London, **227:** 367-380.

APPENDICES

APPENDIX A

TABLES

Table 1. Temperature and chemical composition of Jenn's Pools. All values are in ppm unless otherwise noted.

Jenn's Pools	T (°C)	pH	Eh (mv)	Alkalinity	Total Fe	Fe_2^+	SO_4^{2-}	PO_4^{3-}	NO_3^-	NO_2^-	DO	Cu	Total As
Vent 1	83	5.9	-240	220	0.01	0	130-188	1.50-1.9	4	0.019	0.3-1.8	0	0.1
Vent 2	85	5.9	-240	160-180	0.03	0	124-300	0.35-1.81	0.7	0.025	1.5-1.9	0	NA

Table 2. XRD analysis of sinters and sinter substrate from Jenn's Pools.

Location	sample	subsample	opal-A	opal-CT	quartz	S°	gypsum	jarosite	pyrite	marcasite	greigite	magnetite
Jenn's Pools												
Vent 1	**JK03-006**	ppt on spicules	X	X	X	X	X					
		green spicules	X	X?	X							
		light gray interior										
		black bottom							X			
		orange bottom	X									
		interior							X			
	JK03-007	crust	X	X?	X							
		gray under crust							X			
		off white grain							X			
		white middle							X			
		white side	X									
		fracture							X			
		dark bottom			X				X	X		
	JK03-008	spicules + laminations	X	X	X	X			X			
		dark bottom							X			X
	JK03-018	vent	X	X	X	X		X				
vent 2	**JK03-032a**	crust	X		X	X						
		spicules	X		X	X				X		
		black rock	X			X			X	X		
		crust with organics	X	X	X							
	JK-03-032b	crust plus spicules	X	X					X	X		
		black rock	X	X		X			X	X		
	JK03-033	crust	X		X	X	X		X		X	X
		black rock	X	X	X				X			

Table 2 (*continued)*

Location	sample	subsample	hematite	kaolin group	Halloysite	calcite	dolomite	andesine
Jenn's Pools								
Vent 1	**JK03-006**	ppt on spicules						
		green spicules		X			X	X
		light gray interior		X				
		black bottom		X				
		orange bottom						
		interior		X				
	JK03-007	crust						X
		gray under crust		X				
		off white grain		X-poor ordered				
		white middle		X-well ordered				
		white side		X				
		fracture		X				
		dark bottom		X				
	JK03-008	spicules + laminations				X		
		dark bottom		X	X			
	JK03-018	vent						
Vent 2	**JK03-032a**	crust						
		spicules						
		black rock						
		crust with organics	X				X	X
	JK-03-032b	crust plus spicules					X	
		black rock						
	JK03-033	crust						
		black rock						

Table 3. TGA/DTA data from sinters in Jenn's Pools.

Sample	Kaolinite		sulfur		gypsum		absorbed water	dehydroxylation of opal	
	peak temp	weight loss %	peak temp	weight loss %	peak temp	weight loss %	weight loss %	peak temp	weight loss %
Jenn's Pools									
VENT 1									
JK03-006 gray crust	462	7.3					6.0		
JK03-006 green spicules	472	2.8					7.0		
JK03-006 ppt on spicules			166	0.8	123.0	1.1	6.3		
JK03-007 crust							5.7		
JK03-007 gray crust	475	4.3					2.0		
JK03-007 white middle	459	10.8					1.8		
JK03-008 crust			175	N/A			3.6		
VENT 2									
JK03-032a crust			171	1.2			6.0	252	0.9
JK03-032a spicules							4.8		
JK03-032b crust+spicules							1.3		
JK03-033 crust	483	5.4	165	3.9	124.0	1.4	5.0		

Table 4. Mineralogy of sinter by EDS

Mineral Phase	**Vent 1**	**Vent 2**
Opal*	X	X
Barite*	X	X
Pyrite*	X	X
Iron sulfide*	X	X
Iron oxide*	X	
Titanium oxide	X	X
Ilmenite	X	
Carbonate*	X	
Witherite	X	X
Chromite	X	
Gold*	X	
Halides	X	
Manganese oxide*	X	
Cassiterite	X	
Pyroxene	X	

* mineral phase of known BIM and/or BCM

Table 5. Mineralogy of sinter substrate by EDS and XRD

Mineral Phases identified by EDS	**Vent 1**	**Vent 2**
Opal*	X	X
Kaolinite	X	X
Halloysite	X	
Pyrite*	X	X
Cinnabar	X	
Barite*	X	X
Titanium oxide	X	X
Ilmenite	X	
Carbonate*		X
Witherite	X	
Minamiite		X
Additional Mineral Phases identified by XRD		
Opal-CT		X
Quartz	X	
Marcasite*	X	X
Magnetite*	X	
Jarosite**	X	

* mineral phase of known BIM and/or BCM
** rock sample located within vent; not a sinter

Table 6. TEM observations for mats sectioned from Jenn's Pools.

Sample	Color of mat	Next to sinter/spicules	Location of subsample	External mineralization*	Internal mineralization	Cell morphology	EPS	Internal membranes	Gram (-)	Mineralogy
VENT 1										
JK04-018	Green	Yes- sinter		No	Yes- spheres	various cocci-cells in bad shape	N/A	No	N/A	N/A
JK04-019-a1	Green	Yes- sinter	Edge of mat	Yes- H	No	Mostly cocci Some bacillus Rare segmented	N/A	No	N/A	Amorphous silica
JK04-019-a2	Green	Yes-sinter	Below a1, closer to edge of mat	Yes- M	No	Mostly cocci More segmented	Yes	Yes	N/A	Amorphous silica
JK04-019-a3	Green	Yes- sinter	Below a2, opposite edge of mat	Yes- M to T Some unmineralized	Yes	Mostly cocci More segmented?	Yes	Yes	N/A	N/A
JK04-019-a4	Green	Yes	Below a2	Yes- M to T	No	Mostly cocci	Yes	No	N/A	N/A
JK04-019-b1	Green	No- Next to JK04-019		Yes- T Most unmineralized	No	Mostly cocci Some segmented	Yes	Yes ~ 95%	Yes	N/A
JK04-019-b2	Green	No	Below b1	Yes- T Most unmineralized	Yes	Mostly cocci Some segmented	N/A	? unstained hard to tell	N/A	N/A
JK04-019-c1	Green or tan	Yes- next to sinter but in different region then JK04-019a		Yes- T	No	Mostly cocci some bacillus and filamentous	Yes	Yes- some	Yes	Amorphous silica
JK04-019-c2	Green or tan	Yes	Below c1	Yes- T More than c1	?	Cocci and bacillus	Yes	No	Yes	Amorphous silica

JK04-020a	Pink to tan	Suspended material		Rare	No	segmented cocci bacillus	Mostly yes	Yes	Yes	N/A
JK03-037a	Light Green	Yes- between spicule		Some-T	No	Cocci	Yes	No	No	Amorphous silica
VENT 2										
JK04-24a	Green	Yes- attached to spicule		No	No	Mostly cocci Segmented and/or chained	Yes and No	Some	N/A	N/A
JK04-024b	Green	Yes- attached to spicule	Below a	Some- T	Yes	Cocci	N/A	Yes	No	External- iron oxide Internal- iron oxide and iron sulfide
JK04-025	Pink and white filamtments	loose mat		No	Yes?	Mosly cocci Bacillus	No	Yes	N/A	N/A
JK03-036	Green	Suspended material		Yes	No	No live cells, molds cocci	No	No	N/A	N/A

* H= highly, M= moderately, T=thinly
N/A= not available

APPENDIX B

TGA CURVES

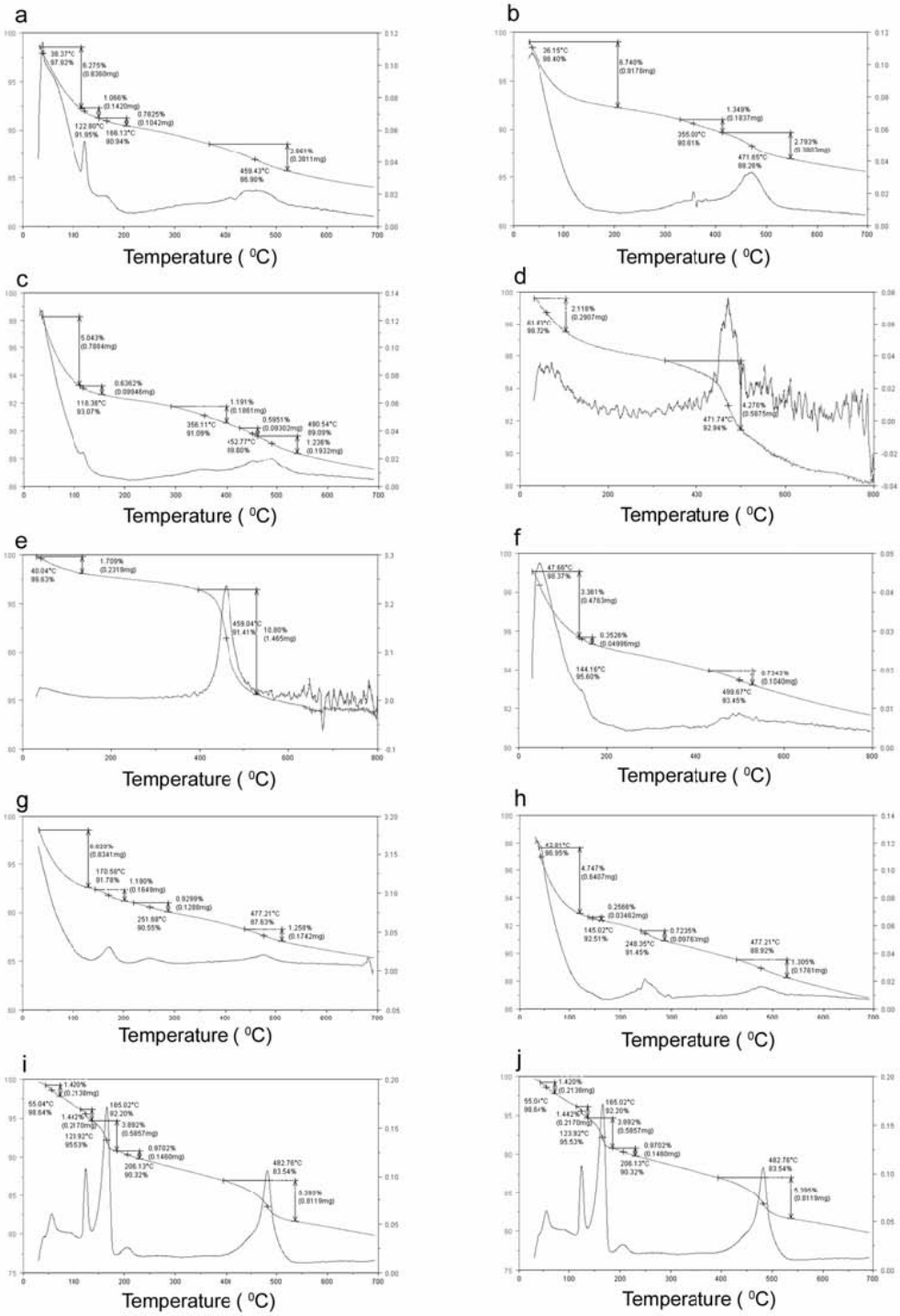

Figure 21. TGA curves of sinters and underlying rocks for Vent 1 (a-f) and Vent 2 (g-j). Left axis is weight (%) and right axis is derivative weight (°C / %) (a) JK03-006 of precipitate on spicules, (b) JK03-006 green spicules, (c) JK03-007 crust (sinter), (d) JK03-007 gray crust (underlying rock), (e) JK03-007 white middle of underlying rock, (f) JK03-008 crust (sinter), (g) JK03-032a crust (sinter), (h) JK03-032a spicules, (i) JK03-032b crust plus spicules, and (j) JK03-0033 crust (sinter).